Available online at www.sciencedirect.com

ScienceDirect

Advances in Space Research 68 (2021) 1243–1262

ADVANCES IN SPACE RESEARCH (a COSPAR publication)

www.elsevier.com/locate/asr

Deep learning model for predicting daily IGS zenith tropospheric delays in West Africa using TensorFlow and Keras

Samuel Osah *, Akwasi A. Acheampong, Collins Fosu, Isaac Dadzie

Department of Geomatic Engineering, Kwame Nkrumah University of Science and Technology, PMB KNUST, Kumasi, Ghana

Received 10 September 2020; received in revised form 5 March 2021; accepted 22 April 2021
Available online 4 May 2021

Abstract

Accessibility and precise modelling of tropospheric delay play a significant role in the precise Global Navigation satellite system (GNSS) positioning applications as well as meteorological studies and weather forecasting. However, if in the event that a GNSS Continuously Operating Reference Station (CORS) is inaccessible due to power outages, poor internet connectivity, equipment failure, and firmware issues, gaps are created in the data archive, and the quality of the tropospheric delay estimation is degraded. Over the years, several modelling approaches and methodologies have been proposed towards the precise estimation of tropospheric delay, owing to the spatiotemporal variability of water vapour content in the atmosphere. This study employs Deep learning (DL) approach with TensorFlow and Keras to develop a predictive model (DLztd) for predicting daily IGS final ZTDs over four selected IGS stations in West Africa. Daily surface meteorological parameters (Pressure (P), Temperature (T), and Water vapour partial pressure (e)), as well as daily ZTD and stations' coordinates (latitude, and ellipsoidal height) obtained from the site-wise VMF3-ZTD products for the period 2015–2018, were used as input variables to train and test the model, while data from 2019 were used to evaluate the predictive performance of the developed model. Statistical performance indicators such as Mean Bias (MB), Root Mean Squared Error (RMSE), Mean Absolute Percentage Error (MAPE), coefficient of determination (R^2), Nash-Sutcliffe coefficient of Efficiency (NSE), and the fraction of prediction within a Factor of Two (FAC2) were employed to determine the degree of agreement between the DLztd model predictions and IGS final ZTD data. The results from the various analyses indicate exceptionally good prediction capability of the DLztd model with average MB, RMSE, MAPE, R^2, NSE and FAC2 of 3.25 mm, 9.62 mm, 0.30%, 0.959, 0.947, and 1.00 respectively. This demonstrates that the DLztd model provides a remarkable alternative for improving the availability of the ZTD data over the IGS stations under study should the stations' data be inaccessible or unavailable.

Keywords: Deep Learning; GNSS; Performance Measures; Vienna Mapping Functions 3 (VMF3); Zenith Tropospheric Delay (ZTD)

1. Introduction

Global Navigation Satellite System (GNSS) signals suffer from the influence of the tropospheric delay originating from the earth's neutral atmosphere. The tropospheric delay induces an excess propagation path length on GNSS signals when transmitting through the troposphere, resulting from signal bending and time delay on account of refraction along the signal transmission path (Mendes, 1999). The excess path length introduces an error in the measured range and the end, degrades the positioning accuracy, particularly the vertical component (Nikolaidou et al., 2018).

The impact of the tropospheric delay on GNSS signals is in the range of about 2.0 to 2.6 m in the zenith direction to about 20 to 28 m near the horizon and at lower elevation angles (Sanlioglu and Zeybek, 2012). Since the tropo-

* Corresponding author.
E-mail address: osahsamuel@yahoo.ca (S. Osah).

https://doi.org/10.1016/j.asr.2021.04.039
0273-1177/

spheric delay cannot be removed by a combination of dual or multi-frequency GNSS observations owing to its non-dispersive nature (not frequency-dependent), unlike the ionospheric delay, the tropospheric delay is considered as the major error source in GNSS positioning applications, and therefore, remains a major challenge and a growing concern to GNSS users. Precise and accurate modelling and/or mitigation of tropospheric delay is therefore essential for precise positioning and navigational applications. Moreover, precise estimates of tropospheric delay can aid in the derivation and retrieval of precipitable water vapour (PWV) content in the atmosphere with a high spatial and temporal resolution, as means of complementing the conventional techniques (such as radiosonde, water vapour radiometer, etc.) of quantifying the amount of water vapour in the atmosphere (Bevis et al., 1992, 1994). Knowledge of PWV is of great interest/essential for meteorological studies, weather forecasts, and climate monitoring (Suparta and Alhasa, 2015; Bianchi et al., 2016; Jiang et al., 2020).

Recently, with the growing demand for GNSS technology, a dense network of permanent and continuously operating IGS stations have been established and distributed globally with the aim of using GNSS measurements provided by these stations for many applications apart from position, such as remote sensing of water vapour in the atmosphere for weather prediction and monitoring (Hadas et al., 2017). However, due to the spatiotemporal variability of water vapour content in the atmosphere, the precise modelling of the tropospheric delay has become an important field of research among the GNSS research community (Hofmann-Wellenhof et al., 2008). This challenge has inspired several techniques and models over the years towards the estimation and mitigation of tropospheric delay (Jiang et al., 2020). The models can be classified into two main groups: surface meteorological parameters dependent models (Hopfield, 1969; Saastamoinen, 1972; Black, 1978) and, user location and time-dependent models (Penna et al., 2001; Leandro et al., 2008; Landskron and Böhm, 2018). Lately, the application of other techniques such as Precise Point Positioning (PPP) (Zhu et al., 2010; Hadas et al., 2013; Zhao et al., 2018), Artificial Neural Network (ANN) (Yang et al., 2017; Ding and Hu, 2019; Zhang et al., 2020), Adaptive Neuro-Fuzzy Interference System (ANFIS) (Suparta and Alhasa, 2013, 2015, 2016) and Numeric Weather Prediction (NWP) models (Jiang et al., 2020; Ssenyunzi et al., 2020) have also been employed to model and predict the tropospheric delay in the zenith direction (ZTD).

The IGS likewise employs PPP technique to provide high-quality continuous daily time series ZTD products at an accuracy of about 4 mm for all IGS ground sites using data in rinex format generated by each IGS site (Byun et al., 2005). Due to the high quality of the IGS-ZTD product, it is been utilized as the standard reference for validating the performances of other ZTD models or products and also the retrieval of PWV for research and meteorological applications (Yao et al., 2018a,b; Ding and Hu, 2019). The quality of the IGS-ZTD estimates depends on the quality and continuous daily data archive at the various IGS ground-stations (Byun et al., 2005). However, if for some reasons such as poor internet connectivity, equipment failure, and electrical power problems (Isioye et al., 2015; Ssenyunzi and Oruru, 2019), the IGS ground-sites are inaccessible or absent, gaps are created in the data archive due to inconsistency in data streaming, and the quality of the tropospheric delay estimation is degraded (Jgouta et al., 2016), which as well inhibits the quality and continuous retrieval of the PWV by the IGS sites.

The African IGS ground sites besides being limited in number, are also noted for having large data gaps (Walpersdorf et al., 2007; Isioye et al., 2015; Ssenyunzi et al., 2020), as provided in Fig. 3, and therefore lack providing continuous daily data which is resourceful and adequate to provide high spatial and temporal resolution ZTD data. Thus, the accurate quantification of ZTD is still a challenge in West Africa. Therefore, the need to investigate alternative methods for predicting ZTD to augment/improve the continuous availability of ZTD data at the IGS stations in West Africa is very crucial.

This paper proposes to build a Deep Learning ZTD (DLztd) model with TensorFlow and Keras to address this challenge in the West African region for predicting daily IGS final ZTDs, which can as well be utilized as an alternative source to improve the availability of the IGS-ZTD data should the stations' ZTD data be inaccessible or unavailable. The findings of this study will go a long way in addressing data gaps issues with the West African IGS stations and also enhance research on GNSS and meteorological applications in the region, which has seen limited studies in these disciplines due to the limited GNSS network and large data gaps. To realize this, the site-wise operational Vienna Mapping Functions 3 (VMF3) ray-traced ZTD products (ZTD, Pressure (P), Temperature (T), and water vapour partial pressure (e)) for global IGS stations as well as the stations' coordinates [latitude (φ) and ellipsoidal height (h)] are used as input and the predictive performance of the model is evaluated using several statistical evaluation metrics based on a one-year (2019) IGS final ZTD data over four selected IGS stations in West Africa.

Lately, Numeric Weather Models (NWM) such as the European Centre for Medium-Range Weather Forecasts (ECMWF), the United States National Centres for Environmental Prediction (NCEP) or National Centre for Atmospheric Research (NCAR) reanalysis data have operationally become an important source of atmospheric data for modelling ZTD by many research institutes and groups as a means of improving space geodetic techniques such as GNSS (Hobiger et al., 2008; Urquhart et al., 2014; Li et al., 2020; Zhou et al., 2020). The Vienna Mapping Functions (VMF: VMF1 and VMF3) service, formally the Global Geodetic Observing System (GGOS) atmosphere project

developed at the Vienna Technical University (TU Wien), is one such institution. The VMF service, among other products, offers daily continuous site-specific ray-traced zenith tropospheric delays (ZHD, ZWD), surface meteorological parameters (P, T, and e) and mapping functions derived from the ECMWF ERA-40 (for VMF1) and ERA-Interim (for VMF3) reanalysis data at 6 h daily and 4 epoch (00, 06, 12 and 18 UT) temporal resolution for IGS stations worldwide. VMF3 is the successor of VMF1, the most widely used product. The precision and accuracy of the VMF service products have been investigated and validated against the IGS zenith delays by a number of researchers (Yao et al., 2017, 2018a,b) to be accurate enough for tropospheric delay mitigation and models evaluation. Tropospheric delay models have also been developed out of the service products. For example, Yao et al. (2018)a,b analyzed the temporal and spatial variations of the GGOS atmosphere data and built a new global ZTD model (GZTD) using spherical harmonic function. Likewise, Sun et al. (2017) also derived a global ZTD simplified model (GZTDS) with the assumption that the troposphere is a nonlinear system using the GGOS Atmosphere data. Ding and Hu (2019) also utilised the GGOS Atmosphere data to develop an ANN technique-based ISAAS model over Russia. In addition, the VMF1 mapping functions have been reported as the most accurate mapping functions to date (Tesmer et al., 2007; Landskron and Böhm, 2018) and their use is recommended for high-precision geodetic applications by the International Earth Rotation and Reference Systems Service (IERS) (Urquhart et al., 2014; Nikolaidou et al., 2018; Feng et al., 2020), and also for all precise geophysical applications (Boehm and VanDam, 2009). All these studies clearly indicate the robustness and reliability of the VMF service products for use in GNSS applications. Hence, making it a good source of data for use in the DLztd model development.

Several studies have successfully implemented ANNs and ANFIS techniques in the prediction of ZTD, which demonstrated good results. For example, Pikridas et al. (2010) developed an ANN-based ZTD model for predicting ZTD over some selected EUREF Permanent GNSS Network (EPN) stations. The predicted results showed a mean bias ranging from −10.9 cm to 11.5 cm and RMSE of 3.6 cm. Zheng et al. (2015) also employed the same technique to develop a regional ZTD prediction model over Jiangsu Province of China, providing a RMSE of 0.004 m. Likewise, Ding et al. (2016); Ding and Hu (2019) also established an ANN-based ZTD prediction model over Russia using ground-based GNSS-ZTD data. The predicted results gave a bias of −4.4 mm and RMSE of 20.4 mm. Correspondingly, Yang et al. (2017) used the backpropagation Neural Network (BP NN) technique to develop a regional ZTD model using 15 Continuously Operating Reference Stations (CORS) in Hong Kong. The accuracy of their model was reported to be 1.1 cm. Suparta and Alhasa (2013) proposed an ANFIS model (a technique that combines neural networks and fuzzy inference system) for predicting ZTD using five selected stations in Antarctica and three selected stations in the Malaysia and Singapore regions. The results showed a RMSE of 0.0175 mm. Li et al. (2020) equally proposed a regional ZTD model based on Generalized Regression Neural Network (GRNN). The GRNN model was developed using meteorological data from the European Centre for Medium-Range Weather Forecasts (ECMWF) and the United States National Centres for Environmental Prediction (NCEP). Using the IGS-ZTD product as a reference over 100 globally distributed IGS stations the experimental results showed a mean bias of 9.5 mm and RMSE of 12.7 mm. Nonetheless, limited or no studies have explored deep learning with TensorFlow and Keras to predict ZTD, especially in the West African region. It, therefore, remains a novel approach for the prediction of ZTD using deep learning with TensorFlow and Keras models.

2. Tropospheric delay

The troposphere forms the lower portion of the neutral atmospheric layer up to around 50 km (Meunram and Satirapod, 2019). The effect of the troposphere on GNSS signals is called tropospheric delay, which induces an extra delay on GNSS measurements. Tropospheric delay is a function of the total refractivity (N), which depends on pressure [$P(mbar)$], temperature [(T (K)] and relative humidity [RH ($\%$)] or water vapour partial pressure [e ($mbar$)] along the signal transmission path as well the location of the receiver antenna (Sanlioglu and Zeybek, 2012). The total delay computed in the zenith direction is called the zenith tropospheric /total delay (ZTD), which is the sum of the Zenith Hydrostatic Delay (ZHD) and the Zenith Wet Delay (ZWD). The ZHD accounts for about 90% of the ZTD and can easily be modelled or predicted to sub-millimetre accuracy by empirical prediction models using surface meteorological observations, whereas the ZWD accounts for the remaining 10% of the ZTD and in contrast to the ZHD, it cannot be precisely modelled or predicted due to its large spatial and temporal variability (Younes, 2016; Zhang et al., 2016). The troposphere is characterized as being a non-dispersive medium for radio frequencies up to 15 GHz, hence its effect is independent of GNSS frequencies and therefore affects carrier phase and code measurements equally (Sanz et al., 2013).

Following (Bevis et al., 1992; Mendes, 1999; Kleijer, 2004) the excess propagation path (ΔL_r^t) can be calculated by integration of the refractive index along the signal transmission path, s, from satellite, t to a receiver, r at elevation angle (θ) via the troposphere as:

$$\Delta L_r^t(\theta) = \underbrace{\int_s (n(s)-1)ds}_{\text{Path delay}} + \underbrace{\left[\int_s ds - \int_G dG\right]}_{\text{Signal bending}} \quad (1)$$

Eq. (1) can also be written as:

$$\Delta L_r^t(\theta) = \int_s (n(s) - 1)ds + [S - G] \tag{2}$$

where S is the curved signal path, G is the geometric signal path.

Expressing the signal delay in the zenith direction (i.e., $\theta = 90^{\circ}$), Eq. (2) now becomes:

$$\Delta L = \int_S [n(s) - 1]ds \tag{3}$$

Expressing n in terms of total refractivity N, where $N = 10^{-6}(n-1)$, Eq. (3) can be rewritten as:

$$\Delta L = 10^{-6} \int_s N(s)ds \tag{4}$$

The refractivity (N) can be related to the meteorological parameters (P, T, e) as (Smith and Weintraub, 1953):

$$N = \underbrace{\left[k_1 \frac{P_d}{T}\right]}_{N_d} + \underbrace{\left[k_2 \frac{e}{T} + k_3 \frac{e}{T^2}\right]}_{N_w} \tag{5}$$

where $P_d = P + e$, is the partial pressure of the dry gases *(in hpa)*, k_1, k_2, k_3 are refractivity constants whose values can be inferred from Bevis et al (1994). Re-writing Eq. (4) in terms of ZTD,

$$ZTD = \underbrace{10^{-6} \int_h^{TOA} N_d(h)dh}_{ZHD} + \underbrace{10^{-6} \int_h^{TOA} N_w(h)dh}_{ZWD} \tag{6}$$

where, h is the height of the station or receiver antenna, and TOA is the top of the atmosphere.

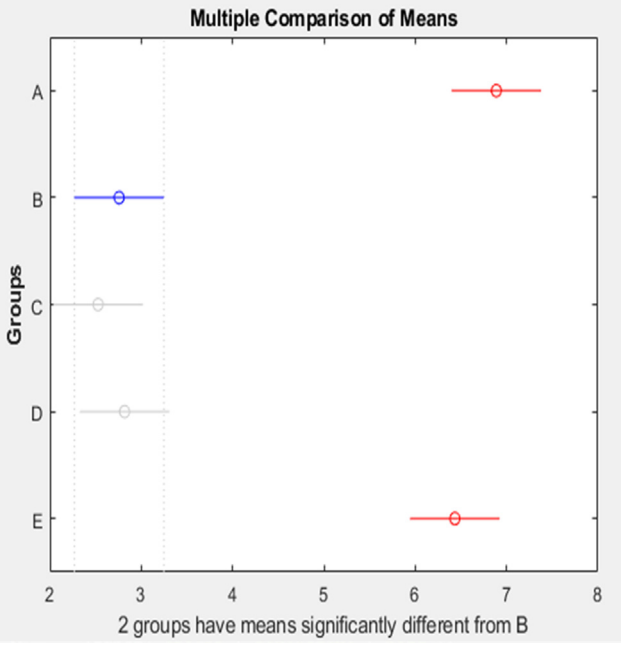

Fig. 1. Sample graph of multiple comparisons of group means. The small circle symbols represent the group means, while the bars (horizontal lines) represent the comparison intervals.

With an appropriate mapping function and using the satellite elevation angle(θ) as input, the ZTD can be resolved into the Slant Tropospheric Delay (STD) as (Landskron and Böhm, 2018):

$$STD_r^t = ZHD \times MF_h(\theta) + ZWD \times MF_w(\theta) \tag{7}$$

where MF_h and MF_w represent the hydrostatic and wet mapping functions.

ZWD can then be converted to PWV for meteorological applications using a conversion factor pie (Π) as (Bevis et al., 1994):

$$PWV = \Pi * ZWD \tag{8}$$

Π is dimensionless and can be determined from (Askne and Nordius, 1987) as:

$$\Pi = \frac{10^6}{\left(\frac{k_3}{T_m} + k_2'\right)\rho_w R_w} \tag{9}$$

where R_w is the specific gas constant for water vapour (461.5 $JKg^{-1}K^{-1}$), ρ_w is the density of water (998 kgm^{-3}), T_m is the weighted mean temperature in kelvin(K), k_2' is refractivity constant (16.52 K/hpa).

3. Materials and methods

3.1. Study area

This study was conducted using four IGS stations located in four West African countries, namely, Benin (BJCO), Cote d'Ivoire (YKRO), Senegal (DAKR) and Cape Verde (CPVG). The West African region lies between latitudes 0°N and 25°N and longitudes 20°W and 20°E. Details of the stations and their visual locations are shown in Fig. 2 and Table 1 respectively.

3.2. Datasets

For effective and efficient data training using deep learning algorithm, this study utilized the daily site-wise operational VMF3 ZTD products for IGS stations and the IGS final ZTD product for a period of five years spanning from 2015 to 2019. The following subsections summarize the datasets used in this study.

3.2.1. VMF3-ZTD data

The Vienna Mapping Functions (VMF) service (https://vmf.geo.tuwien.ac.at/) provides both gridded and site-wise ray-traced VMF1 and VMF3 tropospheric products as open access data for global and more than 500 IGS site users. They are derived based on ray-traced delays at 3° elevation using NWP model data spanning 2001 to 2010 from the European Centre for Medium-Range Weather Forecasts (ECMWF) ERA-40 and ERA-Interim reanalysis data respectively (Putri et al., 2020); and are provided every 6 h daily at four epochs (00, 06, 12 and 18 UT) and 23 h UT the next day (Boehm et al., 2009). VMF3 is the successor

Fig. 2. Map of West Africa showing the locations of the selected IGS stations (GoogleMap, 2021). The red round markers indicate the IGS stations. (For interpretation of the references to colour in this figure legend, the reader is referred to the web version of this article.)

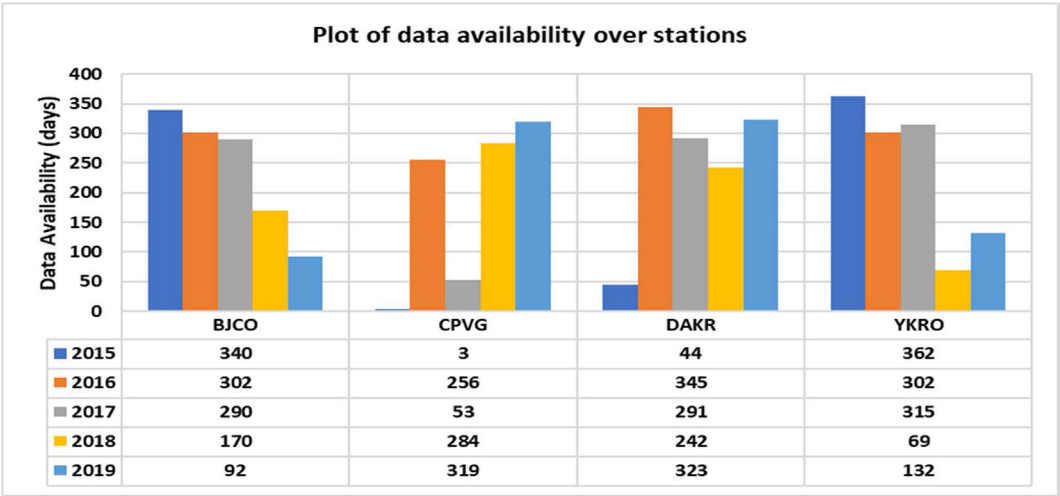

Fig. 3. Data availability (in days) for the IGS stations in West Africa from 2015 to 2019, indicating the stations' varying performances of data acquisition.

Table 1
IGS stations in West Africa selected for this study.

Site	City	Country	Latitude	Longitude	Ellip. Height	Period of data
BJCO	Cotonou	Benin	6.3847°N	02.4500°E	30.700 *m*	2015–2019
YKRO	Yamoussoukro	Cote d'Ivorie	6.8706°N	05.2401°W	270.000 *m*	2015–2019
DAKR	Dakar	Senegal	14.7212°N	17.4395°W	51.000 *m*	2015–2019
CPVG	Espargos	Cape Verde	16.7321°N	22.9349°W	94.089 *m*	2015–2019

of VMF1 realized on both 1° x 1° and 5° x 5° global grids (Landskron and Böhm, 2018). The site-wise VMF3-ZTD data fields for the IGS stations include ZHD, ZWD, P, T, e, and mapping function coefficients (ah) and (aw) for both hydrostatic and wet components respectively. The ZTD is obtained by adding the ZHD and ZWD. The

VMF3-ZTD data is available at: (https://vmf.geo.tuwien.ac.at/trop_products/GNSS/VMF3/).

3.2.2. IGS-ZTD data

The IGS also publishes highly accurate daily final ZTD products based on PPP techniques combined with IGS final orbit and clock solutions for all IGS ground-based tracking stations with an accuracy of about 4 mm. The zenith delays are computed at an interval of 5 min from the IGS stations and are released with 4 weeks latency (Byun et al., 2005). The IGS-ZTD data is available at ftp://cddis.nasa.gov/gnss/products/troposphere/zpd/

3.3. Data extraction

The downloaded daily datasets were extracted into Microsoft Excel for easy exploration and analysis. The extractions were done using coded scripts or m-files written in MATLAB programming language for this study. The extractions were done using coded scripts or m-files, "read_vmfGNSS.m" and "ReadIGSTrop.m" written in MATLAB programming language for this study. For the VMF3-ZTD data, the "read_vmfGNSS.m" m-file was used to extract all the needed parameters in the data file. Parameters extracted were ZHD, ZWD, P, T, and e for each epoch (00, 06, 12, and 18 UT) daily and the first epoch (00 h UT) the next day to obtain complete data for 24 h or 23 h UT. The ZTD was obtained following Eq. (9). No interpolation or extrapolation was performed, since the site-wise parameters are computed at station height and, therefore, no extrapolation was required to transfer from grid height to station height. To obtain the daily (24 h) average datasets, the mean of each daily parameter (ZTD, P, T, e) extracted were computed by summing all the daily epochs (00, 06, 12, and 18 UT) and the first epoch (00 h UT) the next day, and dividing by 5 as given in Eq. (10). The station coordinates for which these parameters are valid were as well extracted from the station coordinate file, "***gnss.ell***".

$$V = \frac{v_{00} + v_{06} + v_{12} + v_{18} + v_{00\ \mathrm{nextday}}}{5} \tag{10}$$

where V is the computed average parameter of interest, v is the parameter of interest, 00, 06, 12, 18 are the daily epochs, and 00nextday is the first epoch of the following day.

Similarly, the IGS-ZTD data were also extracted using the "ReadIGSTrop.m" m-file. Since the IGS-ZTD is computed at an interval of 5 min (temporal resolution) for each day, the mean ZTD was also calculated for the entire day (24 h) for each file, by summing all the ZTDs at each epoch and dividing by the total number of epochs in the file, presented as:

$$ZTD = \sum_{i=1}^{n} \frac{ZTD_e}{n} \tag{11}$$

where n = 288 is the total number of epochs, ZTDe is the ZTD at each epoch.

For each IGS station, the two datasets (VMF3 and IGS) were compared and the corresponding days of data availability were extracted and sorted for the DLztd model development. The total number of days of data available for each IGS station in a given year within the study period is shown in Fig. 3.

3.4. Development of the DL model (DLztd)

3.4.1. Overview of Deep neural network

Deep Learning (DL) is an evolving subfield of Machine Learning (ML) developed to mimic the structure and function of the human brain neural system so as to learn to perform tasks as humans do. The name DL is derived from the use of Neural Networks (NNs) or Multi-Layer Perceptron (MLP) of multiple hidden layers of non-linear processing units/layers stacked together as shown in Fig. 5. It employs ANN algorithms with high computational efficiency and flexibility to learn and extract complex patterns about data from the relationships hidden within the data, then applies these patterns or pieces of knowledge to unknown data for either regression and classification or clustering analyses. The deepness of the DL model (DLM) is dependent on the number of hidden layers in the model, and the deeper the Deep Neural Network (DNN), the more complex patterns the network can learn (Gulli and Pal, 2017; Prakash and Rao, 2017; Liu and Maldonado, 2018).

Typically, the ANN architecture is composed of three different layers that are sequentially interconnected operating in parallel as seen in Fig. 5. They include the input layer, one or more hidden layers, and the output layer. Each layer is composed of several processing units called neurons or nodes as shown in Fig. 5. A neuron is made up of three fundamental units including the connecting links characterized by its weight w, a summation unit U_k which combines the weighted input signals, and an activation or transfer function F for translating the input signals into output signals. ANN acquires knowledge through training and produces outputs based on the knowledge of the relationship between the input signals within the training data. The input layer obtains the data or signals $x_i(i = 1, 2, ..., n)$from the external environment into the network, which is then distributed to the neurons in the hidden layer where the data through the activation function is manipulated by computing the weighted sum of the input signals (multiply the input values by the weights (initially random) and add a bias term) as presented in Eqs. (13) and (14). Relevant patterns associated with the input data are retrieved and transformed into a higher-dimensional space in the hidden layer, allowing the network to learn complex patterns within the data. For multiple hidden layers, the output of one hidden layer becomes the input for another. The weights within the neurons are fundamental assumptions about how the data in one layer is associated with the data in the subsequent layers. As the network

trains the interconnected weights w_i in Eq. (12) are adjusted to minimize the overall error function ε between the network output (predicted) and the target output (actual observation) until they finally converge on values that precisely represent the meaningful pattern within the data (predicted values become as close as possible to target values). ε is the sum of square errors between the predicted/ANN model output t_i and the actual output O_i, which can be defined as (Malekmohamadi et al., 2011):

$$\varepsilon(w) = \frac{1}{2}\sum_{i=1}^{N}(O_i - t_i)^2 = \frac{1}{2}\sum_{i=1}^{N} e^2 \tag{12}$$

where N is the total number of training patterns.

The output layer then presents the final results or output y_k from the processing as presented in Eq. (14).

Mathematically, the operation of a neuron say k can be expressed as follows (Suleiman et al., 2014; Tosun et al., 2016; Wang et al., 2020):

$$U_k = \sum_{i=1}^{N} w_{ki} \cdot x_i \tag{13}$$

$$y_k = F(U_k + b_k) \tag{14}$$

where x_i is the input variable/signal, w_i is the synaptic weight of the neuron k, b_k is the bias term, F is the activation function, and y_k is the output signal of the neuron k.

In a deep neural network, the neurons are sometimes referred to as "fully connected" networks or "fully connected" layers, implying that a given neuron maintains a connection to all the neurons adjacent to it. In recent times, DL has gained a lot of recognition and proven effective in many fields such as speech and face recognition, image classification (Goodfellow et al., 2016), weather prediction (Weyn et al., 2019), detection of volcano deformation (Anantrasirichai et al., 2019), groundwater estimation from major physical hydrology components (Afzaal et al., 2020), prediction of customer records for future product issues Chandrasekaran (2019) and so forth. It is therefore expedient to extend the concept of DL to modelling zenith tropospheric delay.

3.4.2. Developmental environment and libraries

The Deep Learning ZTD (DLztd) prediction model was developed using PyCharm JetBrains 2019.2, a python integrated development environment (IDE), NVIDIA Nsight HUD Launcher 2019.4 GPU platform, together with the following libraries:

(i) ***Pandas v0.25.1*** - for importing the dataset.
(ii) ***NumPy v1.16.5*** - for mathematical operations.
(iii) ***Matplotlib v3.1.1*** - for plotting graphs.
(iv) ***Scikit-learn v0.21.3*** - a tool for ML.
(v) ***Sklearn:*** for statistical metrics evaluation.
(vi) ***Seaborn v0.9.0*** - for statistical data visualization.
(vii) ***TensorFlow v2.0.0*** - a python-friendly open-source library built with data-flow graphs by the Google Brain team for numerical computation that makes deep and machine learning faster and easier. TensorFlow, therefore, provides an interface for expressing and implementing machine learning algorithms and to execute such algorithms (Abadi et al., 2016).
(viii) ***Keras v2.2.4*** - a powerful, easy-to-use python open-source library that implements Deep Learning algorithms and can run on TensorFlow or Theano as backends (Manaswi, 2018).

3.4.3. Input and output variables

It is established that meteorological parameters such as Pressure, Temperature, water vapour partial pressure as well as station location significantly influence the magnitude of tropospheric delay (Sanlioglu and Zeybek, 2012). Thus, the DLztd model variables including input and output (target) features were selected following (Ding et al., 2016; Ding and Hu, 2019). A ZTD residual inverted by the VMF3-ZTD product with respect to the IGS final ZTD was used as the target variable which can be computed as (Ding et al., 2016):

$$RES = ZTD_{VMF3} - ZTD_{IGS} \tag{15}$$

where RES is the VMF3-ZTD product residual, ZTD_{VMF3} is the VMF3-ZTD, and ZTD_{IGS} is the IGS-ZTD obtained from the IGS stations under study.

RES from Eq. (15) is related to three main parameters: geographical coordinates, latitude φ, and ellipsoidal height (h) of the IGS stations under study; surface meteorological parameters (P, T, e) at the IGS sites, and ZTD values, all extracted from the site-wise VMF3-ZTD data fields. Thus, the RES is determined by all of φ, h, P, T, e and ZTD_{VMF3}. Table 2 provide the list of input and output variables for the DLM.

Table 2
Input and output variables for the Deep learning model (DLztd).

Variable Name	Source	Acronym	Units	Function
Latitude	VMF3	Lat	Deg	Input
Ellipsoidal Height	VMF3	h	m	Input
Pressure	VMF3	P	hpa	Input
Temperature	VMF3	T	K	Input
Water vapour partial Pressure	VMF3	e	hpa	Input
Zenith Total Delay	VMF3	ZTDvmf3	m	Input
Residual	Difference (VMF3 and IGS)	RES	m	Output

The DLztd model was trained and tested on data from 2015 to 2018 while data from 2019 from the four IGS stations (BJCO, CPVG, DAKR, and YKRO) was set aside as an independent dataset (not used in the model development process) for the final model performance evaluation.

3.4.4. The DLztd model development

The following steps were employed in developing the DLztd model which can as well be visualized from Fig. 4:

1) Data pre-processing

The first step in NN training is to identify the datasets, remove noisy data and missing values and other unwanted information in the dataset. This mechanism is referred to as data pre-preprocessing. After ensuring that noisy data and missing values are removed, the next step is to partitioned or split the dataset into a training and a test set which can be done through indexing, creating indices of '1′ and '2′. We split the 2015–2018 data covering all the four IGS stations into 80% of training and 20% of test sets. The network learns from the training dataset and then use the test set to evaluate the model's performance.

2) Feature Scaling/Normalization:

Data scaling or Normalization is the process of making model data in a standard format of say 0′s and 1′s so that the training is improved, accurate, and faster. Scaling is done by calculating the mean and the standard deviation of the training set and then normalizing both the training and test sets using the mean and standard deviation of the training set. The normalization method was implemented using the StandardScaler of scikit-learn using Eq. (16) (Agarap, 2018):

$$z = \frac{x - \mu}{\sigma} \tag{16}$$

where z represents the normalized dataset, x represents the dataset features, μ represents the mean value for each dataset feature x_i, and σ represents the corresponding standard deviation.

3) Model Creation: The 'layers.Dense ()' function was used to define "fully connected" layers and the number of neurons in each layer. The DLztd model consists of a simple sequential layout, an input layer of 6 neurons, representing the number of feature variables in the data, 4 hidden layers with 200, 200, 128, and 54 neurons respectively

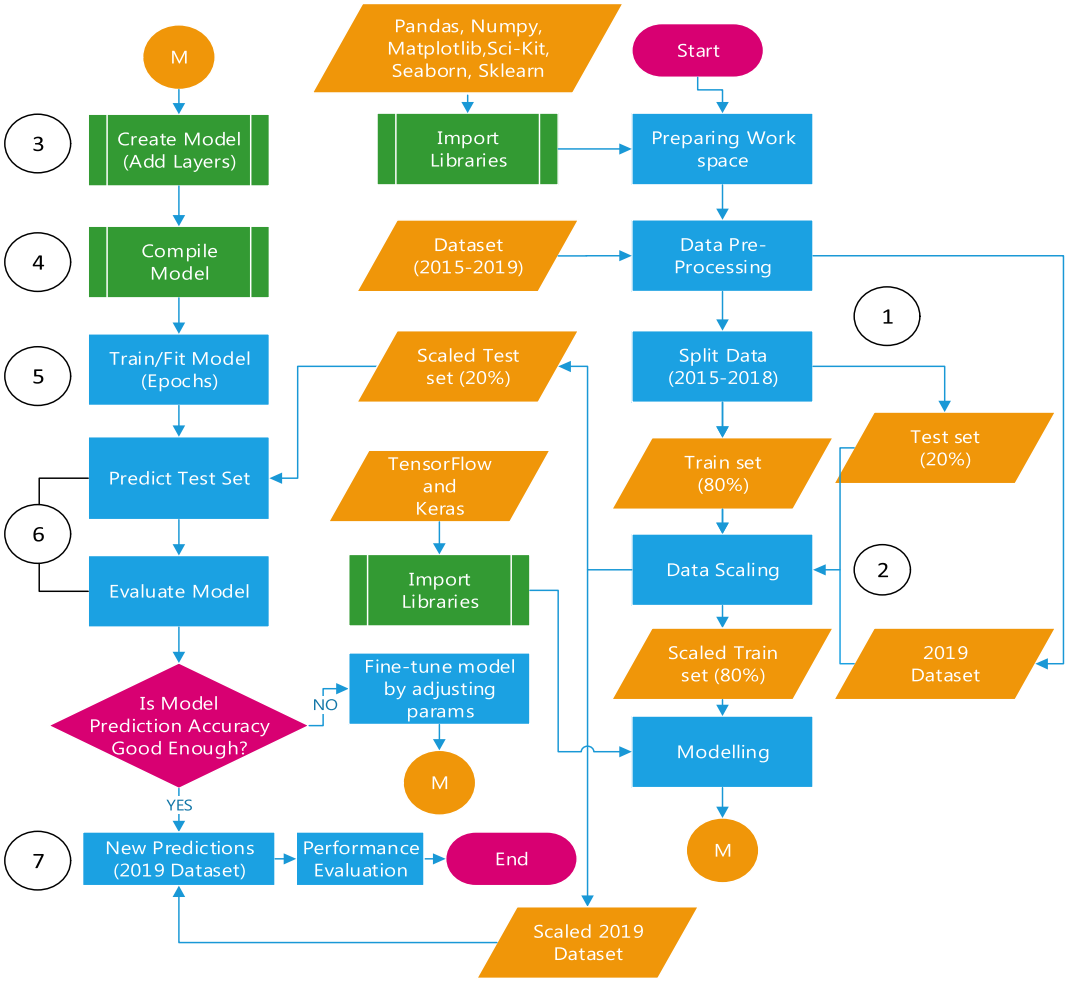

Fig. 4. Workflow methodology of the developed Deep Learning ZTD (DLztd) model. The numbered circles (1–7) represent the various steps taken in developing the DLztd model, as described in Section 3.4.4.

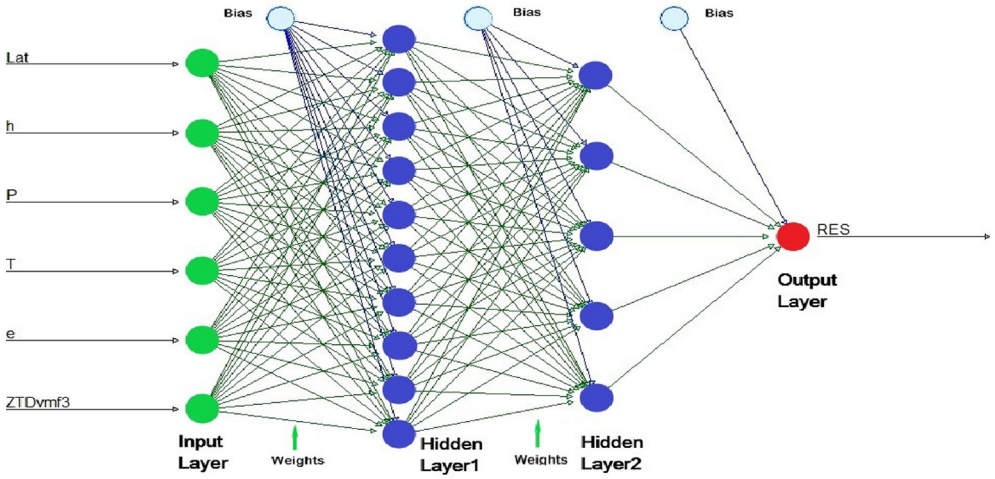

Fig. 5. Sample Deep Learning Architectural design showing the input, hidden, and output layers together with connecting weights and bias. The circles with green colour represent the neurons in the input layer, the blue circles represent the neurons in the hidden layers, and the red circles represent the neurons in the output layer. The connecting arrows between the layers or neurons represent the weights, while the cyan circles represent the bias. (For interpretation of the references to colour in this figure legend, the reader is referred to the web version of this article.)

and an output layer of 1 neuron. Fig. 5 provides a sample architectural design of the DLM. The Rectified Linear Unit (ReLU) activation function is used for each hidden layer neuron. The ReLu function is a piecewise linear function that will output 0 when $\times < 0$, and conversely, it will output a linear function or the input (x) directly when $\times \geq 0$. The equation of the ReLU function is defined as (Agarap, 2018; Wang et al., 2020):

$$f(x) = \max(0, x) = \begin{cases} x, & x \geqslant 0 \\ 0, & x < 0 \end{cases} \tag{17}$$

For several models of neural networks, ReLU has been the widely used activation function (Agarap, 2018). For each hidden layer, a dropout layer is also employed to combat or reduce underfitting (i.e., having worse than possible predictive performance) and overfitting (i.e., being too sensitive to the training data) in the deep neural networks. For the first three layers, a dropout rate of 0.4 (40%) is used while a dropout rate of 0.3 (30%) is used in the last layer. Dropout is a technique that regularizes the behaviour of DNNs during training and helps reduce neuronal interdependent learning (Srivastava et al., 2014; Shirke et al., 2018). Simply put, dropout refers to randomly dropping out or temporarily removing units (hidden and visible) along with all their connections from the network during training. This implies that either in the feed-forward or in the back-propagation phase, their weights will not be changed/modified, and no output from that neuron is generated. Dropout rate expresses the fraction of weight to drop as it determines the probability at which feature detectors are deleted or removed and the remaining weights are trained by backpropagation. For example, a dropout rate set to 0.2 (20%), will mean that one in five inputs will be randomly omitted from each update cycle.

4) Compiling the model: Before fitting the model, the model requires compilation. The loss function, optimizer, and metrics are specified during this step. The DLztd model utilized the Mean Squared Error (MSE) as the loss function, the 'RMSprop' optimizer with a learning rate of 0.001 is used as the optimizer, and Mean Absolute Error (MAE) is used as the metric. The loss function and the metric are used to evaluate the model performance.

5) Fitting the model: The training set is used to fit the compiled model. Besides, a validation set is created during the training and is set to consist of a fraction of '0.2′, of the training data. 1000 epochs are run, with a batch size of 64. The epochs specify the number of times the algorithm considers the entire training data while the batch size specifies the size of the sample to be passed through the algorithm in each epoch. Here again, the early stopping function was implemented to avoid over-and under-fitting.

6) Model Evaluation: Lastly, the trained or fitted model and the test set is used to evaluate the model performance, and loss of 9.3651e-05 m and MAE of 0.0081 m was realized.

7) Prediction of the new dataset: After the model is trained and evaluated on the test data, new predictions for the target variable *RES*, are made on the 2019 datasets from which the DLM ZTD is computed as given in Eq. (18) for the final model evaluation.

The end product of the DLM is the *RES*, therefore, the ZTD prediction follows (Ding and Hu, 2019):

$$ZTD_{DLM} = ZTD_{VMF3} - RES \tag{18}$$

It follows that ZTD_{DLM} is compensation for VMF3-ZTD (ZTD_{VMF3}) with respect to the IGS final ZTD, which directly implies that the *RES* is the compensation for the VMF3-ZTD product.

3.4.4.1. Performance evaluation of the DLztd model. To finally evaluate the performance of the developed DLztd model on the 2019 dataset, statistical analysis involving

the Mean Bias (MB, Eq. (19)), Root Mean Square Error (RMSE, Eq. (20)), Mean Absolute Percentage Error (MAPE, Eq. (21)), Pearson coefficient of determination (R^2, Eq. (22)), Nash-Sutcliffe coefficient of Efficiency (NSE, Eq. (23)), and the fraction of predictions within a factor of two of observations (FAC2, Eq. (24)) (Nash and Sutcliffe, 1970; Kumar et al., 1999; Ali and Abustan, 2014; Sayegh et al., 2014; Suleiman et al., 2014; Ahmadi and Rodehutscord, 2017) was conducted to quantify the extent to which the predicted ZTD values on the independent dataset from the four IGS stations are close to the corresponding true ZTD (IGS) values. The expressions for the aforementioned statistical indicators are represented as follows:

$$MB = \frac{1}{N}\sum_{i=1}^{N}(M_i - O)_i \tag{19}$$

$$RMSE = \sqrt{\frac{1}{N}\sum_{i=1}^{N}(M_i - O_i)^2} \tag{20}$$

$$MAPE = \frac{1}{N}\sum_{i=1}^{N}\left|\frac{M_i - O_i}{O_i}\right| \times 100 \tag{21}$$

$$R^2 = \frac{\left[\sum_{i=1}^{N}\left(M_i - \bar{M}\right) \times \left(O_i - \bar{O}\right)\right]^2}{\left[\sum_{i=1}^{N}\left(M_i - \bar{M}\right)^2\right]\left[\sum_{i=1}^{N}\left(O_i - \bar{O}\right)^2\right]} \tag{22}$$

$$NSE = 1 - \left[\frac{\sum_{i=1}^{N}(O_i - M_i)^2}{\sum_{i=1}^{N}\left(O_i - \bar{O}\right)^2}\right] \tag{23}$$

$$FAC2 = 0.5 \leqslant \frac{M_i}{O_i} \leqslant 2.0 \tag{24}$$

where M_i and O_i represent the *ith* modelled and observed (IGS) ZTDs respectively and, $\bar{M}$ and $\bar{O}$ their respective means. N is the total number of observations.

The performance measures/metrics indicated above. can be categorised into three perspectives (Fox, 1981; Kumar et al., 1999; Ali and Abustan, 2014):

- Measures of difference or error index (MB, RMSE, and MAPE)
- Measures of association or goodness-of-fit (R^2), and
- Measures of efficiency (NSE, and FAC2). These measures or indicators are less common in the GNSS field but widely used in the field of hydrology and other disciplines.

The ***MB*** indicates the average deviation of the DLztd model predictions compared to the observed (IGS) values, where negative and positive MB values indicate under- and over-estimation respectively. MB values range from -∞ to +∞ with zero being the MB value for an ideal model. The ***RMSE*** is a measure of the absolute fit of the DLztd model to the observed (IGS) data. That is to say, it provides an overall measure of how accurately the DLztd model predicts the observe (IGS) values. RMSE values vary between 0 and ∞, with 0 being RMSE for an ideal model. The lower the MB and RMSE values, the less the prediction error, and the better the model fit. The ***MAPE*** similarly indicates prediction accuracy, and measures how much error in predicting compared to the observed (IGS) values expressed in percentage terms. The smaller the MAPE, the better the performance of the model. Accuracy can as well be defined in terms of MAPE as *Accuracy (%) = 100-MAPE (%)*, which is an indication of how close the predicted is to the true (desired) values.

R^2 (R-squared) measures the goodness of fit which describes the proportion of the total variance in the observed (IGS) ZTD values that can be explained by the DLztd model. R^2 varies from 0 to 1 or 0% to 100%, with higher values indicating better performance.

Additionally, **NSE** measures the relative magnitude of the residual variance compared to the variance of the observed data (Nash and Sutcliffe, 1970). According to Chiew and McMahon (1993), NSE provides a more direct measure of the agreement between the observed (IGS) and predicted values than R^2. Legates and Mccabe (2013) finally added that NSE is a necessary quality for any metric of model evaluation. A value of NSE closer to 1 implies that the model can reproduce satisfactorily the observed (IGS) data, with NSE = 1.0 indicating a perfect match of the model predictions to the observed (IGS) values. Furthermore, FAC2 measures the fraction or percentage of the DLztd model's prediction within a factor two of the observed (IGS) values. FAC2 is considered a robust performance measure since it is not overly affected by outliers (Chang and Hanna, 2004). FAC2 value closer to 1.0 infers a closer match between the modelled (DLztd) and observed (IGS) values and, therefore implies better model performance. A perfect model has a FAC2 = 1.

To further investigate the performance of the DLztd model, a non-parametric post-hoc or multiple comparison test (MCT), and graphical techniques were also employed to determine the degree of agreement between the predicted (DLztd) and observed (IGS) ZTD values. According to Biondi et al. (2012), graphical methods provide for qualitative and subjective evaluation and thus represent a fundamental phase in the model assessment as it facilitates the detection of patterns in error occurrence. They are in most cases, based on graphical comparison of predicted (DLztd) and observed (IGS) time series. The following are typical graphical representations used in this study:

(1) Scatterplots , a graphical technique that maps the pairs of prediction and observation to demonstrate how they relate to each other,
(2) Time variation plots , useful tools in describing how the predicted (DLztd) and observed (IGS) ZTDs vary with time (i.e., the hour of the day, day of the week, day of the year (doy), weekly, monthly, yearly etc.),

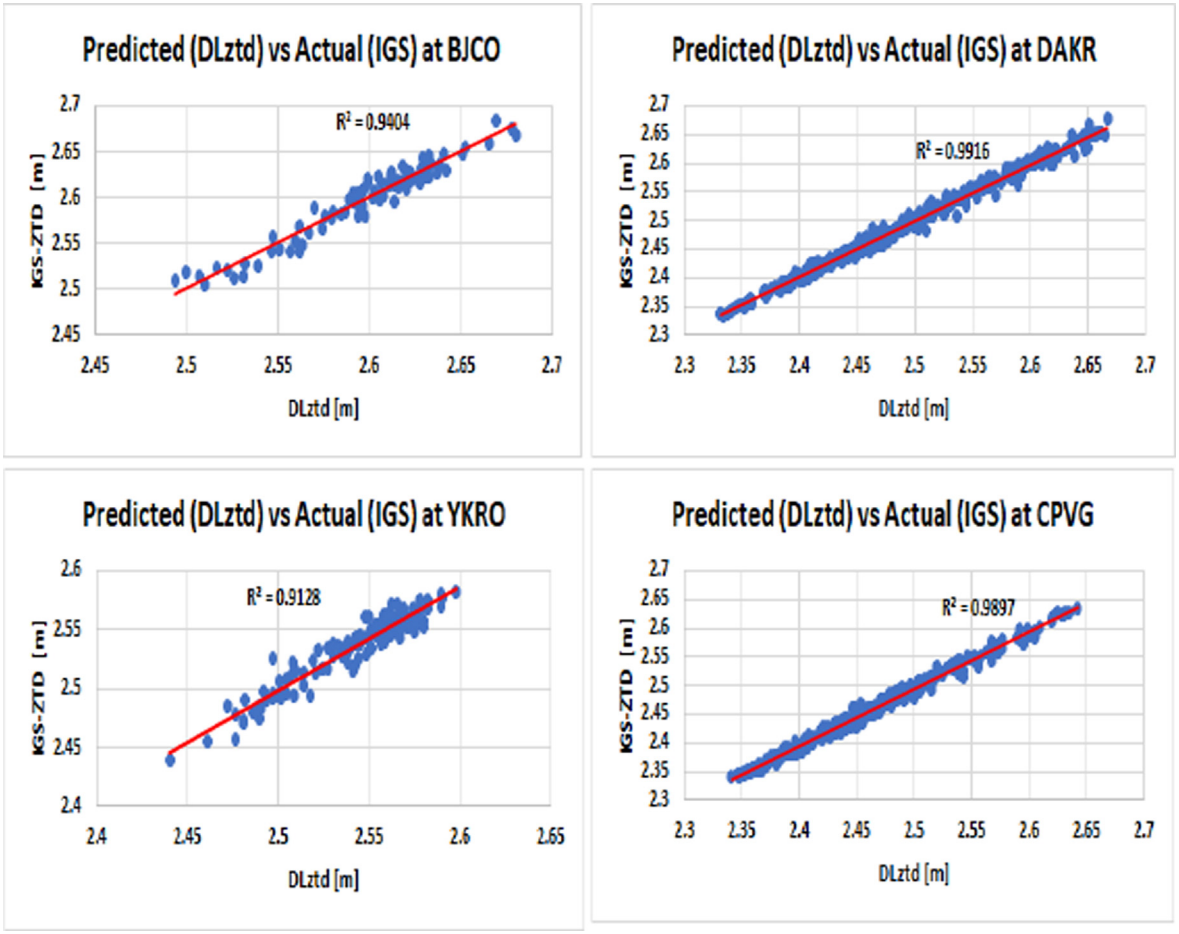

Fig. 6. Scatterplots showing the strength of association between the IGS and DLztd model ZTDs at each IGS station. R2 is the coefficient of determination and the red lines represent the regression lines. (For interpretation of the references to colour in this figure legend, the reader is referred to the web version of this article.)

(3) Residual plots , a graphical technique used to assess the DLztd model adequacy. It is the plot of residuals (observed-predicted) against predicted values to test for linear prediction bias (Ahmadi and Rodehutscord, 2017), and

(4) Taylor's diagram ,a graphical tool developed by (Taylor, 2001) for comparing the performance of different models. It displays three measures of model performance; the coefficient of correlation, standard deviation, and centred RMSE (Suleiman et al., 2014). (Taylor, 2001) demonstrated that these performance statistics can be related using the cosine law in 2D graphs.

The non-parametric post-hoc or multiple comparison test (MCT) was conducted using the 'scheffe' technique (McHugh, 2011; Lee and Lee, 2018) to test whether the difference in the mean values of the DLztd and the IGS-ZTD values is significant at a 5% significant level using Matlab "***multcompare function***". The Null and Alternate hypothesis (H0 and Ha) tests are stated as follows:

H0: The difference between the means is equal to 0.

Ha: The difference between the means is different from 0.

One of the outputs of the MCT using the "***multcompare function***" in MATLAB is an interactive graph that shows the mean of each group represented by a symbol (small circle) and a comparison interval or bar also represented by a line extending from the symbol as shown in Fig. 1. Two groups (e.g., A and B) means are significantly different if their intervals are disjoint and significantly indifferent if their intervals overlap or intersect. For a selected group (e.g., B), the comparison bar is highlighted blue and all other groups that are significantly different are highlighted red (e.g., A and E). The bars for the groups that are not significantly different are highlighted in grey (e.g., C and D) as shown in Fig. 1. It is important to note that Fig. 1 is a sample graph used to explain the MCT and not a graph created in this study.

Thus, the predictive performance of the DLztd model was assessed statistically and graphically centred on 5 possible criteria:

- Measures of difference or error index (MB, RMSE, and MAPE)
- Measures of association or goodness-of-fit (R^2)
- Measures of efficiency (NSE, and FAC2).

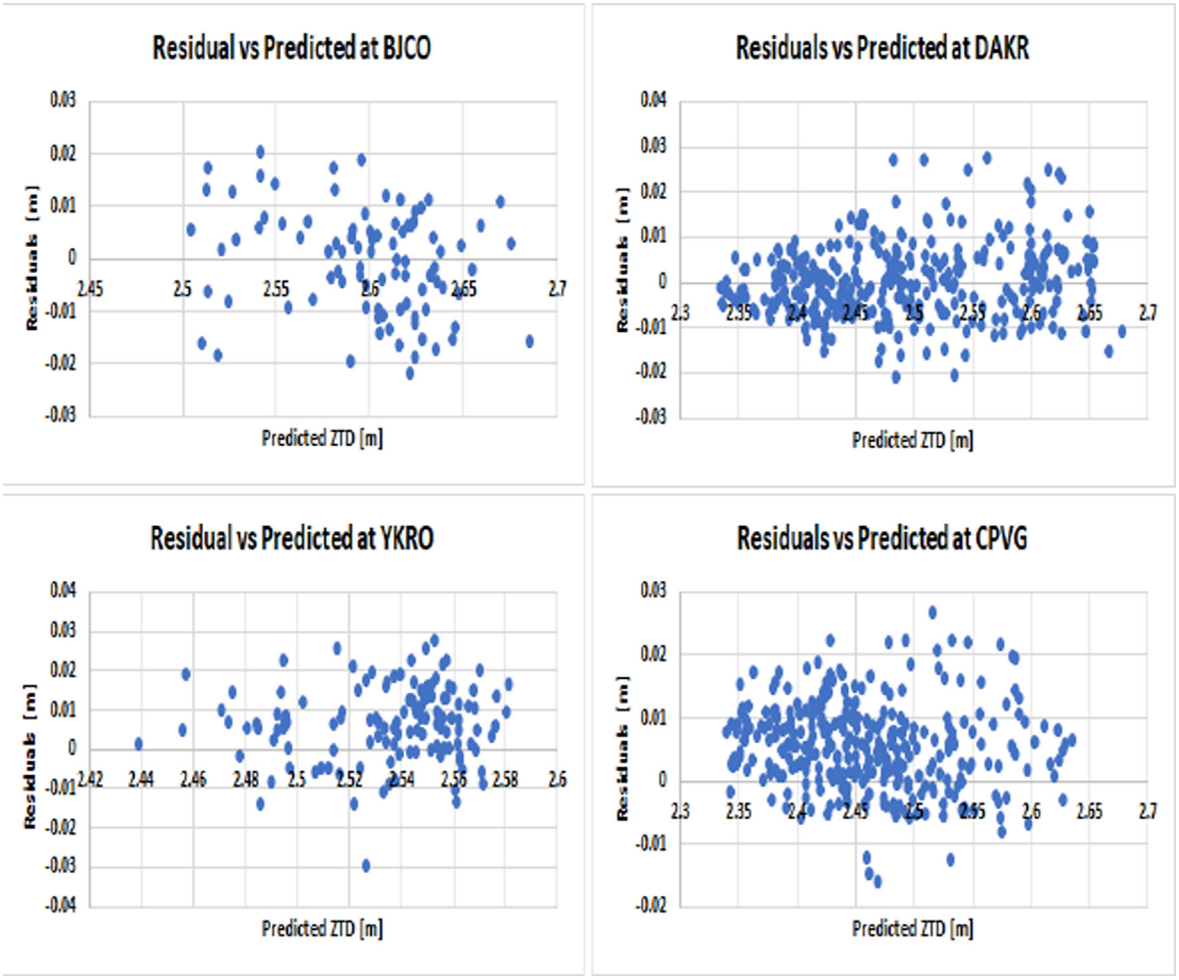

Fig. 7. Plot of residuals against predicted (DLztd) values of ZTD. The DLztd model's prediction is on the x-axis and the accuracy of the prediction (residuals = Observed (IGS)-predicted (DLztd)) is on the y-axis. The distance from the line at 0 (origin) indicates how bad the prediction was for that value. positive values for the residual mean the prediction was too low, and negative values mean the prediction was too high; 0 means the prediction was exactly correct as of the observed.

- Measures of Graphical representations (scatterplots, time variation plots, residual plots, and Taylor's diagram)
- A non-parametric post-hoc or Multiple Comparison Test (MCT).

4. Results and discussion

The objective of this paper is to use Deep Learning with TensorFlow and Keras to develop a reliable ZTD prediction model (DLztd) over four West African IGS stations. The input parameters for the developed DLztd model are surface meteorological parameters (P, T, and e), ZTD, and station coordinates (φ, and h) obtained from the site-wise VMF3-ZTD products. The final model's performance was tested using an unseen dataset of 2019 covering the four IGS stations. The performance statistics of the developed DLztd model using the various statistical indicators; the MB, RMSE, MAPE, R^2, NSE, and FAC2 at each IGS station are summarised in Table 3. In various GNSS applications and tropospheric delay modelling, the ultimate goal is to build models that provide more precise and accurate prediction values of the target variables. Therefore, it is necessary to quantify the extent to which the DLztd model's predictions match the true (IGS-ZTD) values in order to evaluate its predictive performance. The MB and RMSE help to quantify how close the DLztd values are to the true (IGS-ZTD) values. The smaller the MB and RMSE values (closer to zero), the closer the DLztd predictions are to the IGS-ZTD values and the better the DLztd model performance. As can be seen from Table 3, the DLztd model yields smaller MB and RMSE values at all the IGS stations, with the CPVG station having the smallest MB of 0.24 mm and RMSE of 8.22 mm, followed by DAKR with a MB of 0.45 mm and RMSE of 8.84 mm, then BJCO with MB of 5.51 mm and RMSE of 9.87 mm and finally, YKRO which recorded the largest MB of 6.78 mm and RMSE of 11.55 mm. These performance statistics demonstrate a remarkable correspondence between the predicted (DLztd) and IGS ZTD values, and hence better performance. It can further be noted from

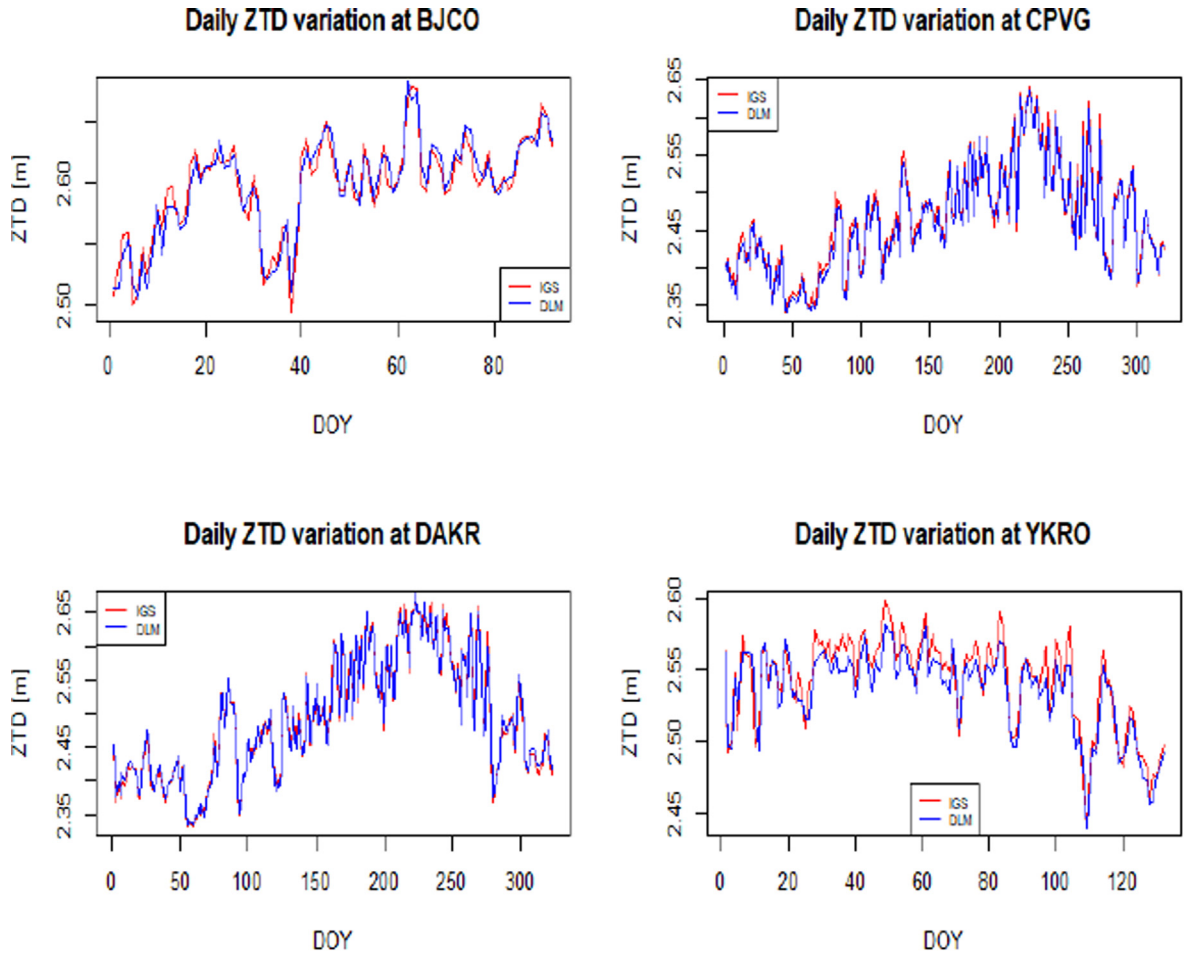

Fig. 8. Daily variation of ZTD estimated from the DLztd model compared with IGS final ZTD data at each IGS station in West Africa for the year 2019.

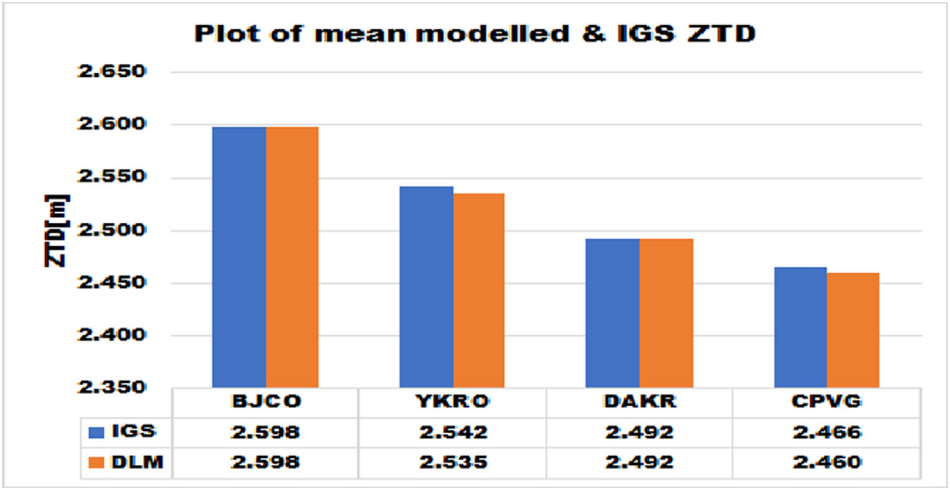

Fig. 9. Comparison of mean predicted (DLztd) and IGS ZTD values over the four selected IGS stations in West Africa.

Table 3 that the MAPE index of the ZTD values estimated by the DLztd model at all the IGS stations is within the interval of 0.25% to 0.38%, implying a high prediction accuracy of the DLztd model. As evidence from Lewis (1982), the threshold criteria indicating a model's high prediction accuracy based on the MAPE index is suggested to be MAPE $\leq$ 10%. 10% $\leq$ MAPE $\leq$ 20% suggests good prediction accuracy, 20% $\leq$ MAPE $\leq$ 50% means acceptable prediction accuracy and MAPE $\geq$ 50% suggests inaccurate prediction.

Table 3
Statistical performance of the DLztd model w.r.t. IGS ZTD values at each IGS station.

Site	MB	RMSE	MAPE	R^2	NSE	FAC2
	[m]	[m]	[%]	[-]	[-]	[-]
BJCO	0.00551	0.00987	0.317	0.9404	0.9366	1.00
YKRO	0.00678	0.01155	0.372	0.9128	0.8722	1.00
DAKR	0.00045	0.00884	0.254	0.9899	0.9863	1.00
CPVG	0.00024	0.00822	0.251	0.9916	0.9913	1.00
Mean	**0.00325**	**0.00962**	**0.299**	**0.9587**	**0.9466**	**1.00**

Additionally, to measure how much of the observed (IGS) variance is explained by the DLztd model prediction, R^2 became a useful tool. As discussed above, the larger the R^2 value the greater the explanatory power and the better the model fit the dataset. The results in Table 3 clearly show that the R^2 obtained by the DLztd model at all the IGS stations ranges between 0.913 and 0.992, indicating that a greater percentage (91.3% to 99.2%) of the total variance in the observed (IGS-ZTD) data has been accounted for by the DLztd model. In accordance with Chiew and McMahon (1993), a model's prediction is considered ideal if $R^2 \geq 0.97$ or $R^2 \geq 0.93$ and acceptable if $R^2 \geq 0.90$ or $R^2 \geq 0.77$. By applying these thresholds criteria, it presupposes that the DLztd model predictions match well with the IGS-ZTD predictions, signifying a higher accuracy of the ZTD prediction. IGS station CPVG had the highest R^2 of 0.992 (99.2% explained) and YKRO had the lowest R^2 of 0.913 (91.3% explained). By way of proof from the scatter plots in Fig. 6, it can be observed very clearly that the data points are closer to the regression lines, which according to Frost (2019) when a model (DLztd) accounts for more of the variance in the observed values (IGS), the data points are closer to the regression line.

Following Abdel-Sattar et al. (2021) and Ahmadi and Rodehutscord (2017), the R^2 value is used as a common criterion to determine the "accuracy" of a particular model based on its prediction while the MB, RMSE, and MAPE are widely used to illustrate the "precision" of a model based on the residual analysis. The use of a variety of indicators to infer and/or compare the overall performance of models is therefore preferred. Therefore, in modelling ZTD based on the DLztd model, the goodness-of-fit in terms of R^2, MB, RMSE, and MAPE showed relatively higher accuracy and precision of prediction, illustrating an exceptional predictive performance.

Not to mention, the fit of the DLztd model was also expressed by NSE and FAC2 as a means of evaluating its predictive power. According to the obtained NSE and FAC2 values (NSE ranging from 0.872 to 0.991 and FAC2 = 1.00) in Table 3, the DLztd model exhibited a phenomenal performance in the prediction of ZTD in the study area, as this is consistent with Chiew and McMahon (1993) and Moriasi et al. (2015) criteria for model classification, that a model is considered perfect for prediction if NSE $\geq$ 0.93, very good if NSE $\geq$ 0.80, and satisfactory if NSE $\geq$ 0.60. IGS station DAKR yielded the highest NSE value of 0.991 while YKRO produced the least NSE value of 0.872. Again, in conformity with (Kumar et al., 1999; Chang and Hanna, 2004; Sayegh et al., 2014; Suleiman et al., 2014), a perfect model reproducing the observed values in terms of FAC2 is defined by FAC2 = 1.0.

Moreover, as a means of visual inspection, the fitness of the DLztd model was evaluated using residuals plots as shown in Fig. 7 to test for prediction bias (Ahmadi and Rodehutscord, 2017). A residual plot is a graph that is used to test the goodness-of-fit in regression and other soft-computing methods. Examining residual plots helps to determine whether the model provided unbiased estimates that appear to be close enough to the observed values. For a good model prediction, the residuals are expected to be randomly distributed around the 0 horizontal lines (origins) showing no defined patterns in the data points. This is to satisfy the assumption that the residuals have a constant variance. Other characteristics of a good residual plot include:

showing a high density of points close to the origin and a low density of points away from the origin, and lastly being symmetric with respect to the origin. It can be seen from Fig. 7 that the residuals are randomly distributed, showing a high density of points close to the 0 horizontal lines (origin) and low-density points far from the 0 horizontal lines. There is also no evidence of clear or recognizable patterns in the residuals as we long the x-axis. This is a measure of good agreement between the observed (IGS) and the predicted (DLztd) ZTD values.

Figs. 8 and 9 further show the daily and mean variations of the observed (IGS) and predicted (DLztd) ZTD values at all the stations, which allow quantitative comparison between the predicted (DLztd) and the observed (IGS) ZTDs at each IGS station. It can be seen from the above-mentioned Figures that the developed DLztd model prediction matches well with the observed (IGS) ZTD values; i.e., the overall trend or pattern is completely consistent, showing a good correlation. This also infers that the DLztd model has successfully modelled the datasets.

To further evaluate graphically the performance of the DLztd model, Taylor's diagram became handy and was plotted for the four (4) IGS stations as shown in Fig. 11. Taylor diagram (Taylor, 2001) provides a visual comparison between modelled and observed values by graphically displaying a statistical summary of how well the model's predictions match the observed (IGS) values in terms of their correlation coefficient (R), centred RMSE and standard deviation (SD). From the various plots in Fig. 11, the position of the coloured symbol (blue) quantifies how closely the DL model predictions at each IGS station match the observed (IGS) values. The black dashed arc in the diagram represents the observed (IGS) standard deviation at the point marked ***"observed"*** on the x-axis. From Fig. 11 the observed standard deviation at the IGS stations can be read as: (BJCO: 0.039 m, YKRO: 0.032 m, DAKR: 0.088 m, and CPVG: 0.068 m). The red

contours indicate the centred RMSE between the modelled and observed (IGS) values, which is proportional to the distance to the marked point ***"observed"*** on the x-axis. The standard deviation of the predicted ZTD values is proportional to the radial distance from the origin and the correlation coefficient is clearly shown as the black arc with the marked graduated values (0.1–0.99) in Fig. 11. The three measures of model performance at the four IGS stations can be read from Fig. 11 as: BJCO (RMSE: 0.01 m, SD: 0.04 m, R: 0.97), YKRO (RMSE: 0.011 m, SD: 0.029 m, R: 0.96), DAKR (RMSE: 0.008 m, SD: 0.086 m, R: 0.99), and CPVG (RMSE: 0.008 m, SD: 0.068 m, R: 0.99). Predictions that match well with the observed values will lie nearest or exactly on the black arc or the ***"observed"*** marked point having high correlation and low RMSEs. It can be deduced from Fig. 11 that the DLztd model values at all the stations agree best with the IGS ZTD values with IGS stations CPVG and DAKR having the best match with almost the same smaller RMSE and high R values. Station CPVG, however, has almost the same SD as the observed, whereas station DAKR has a slightly lower SD than the observed. IGS stations BJCO and YKRO on the other hand, have about the same RMSE and R. BJCO however, showed slightly higher SD while YKRO showed slightly lower SD compared to the observed SD.

Again, the results of the multiple comparison test (MCT) is shown in Fig. 12. As already indicated, the MCT was performed to test whether the difference in the mean values of the DLztd and the IGS-ZTD is significant at 5% significant level. The MCT as shown in Fig. 12 indicates that the mean ZTD of group 1 (IGS) in blue is not significantly different from group 2 (DLM) at the 5% significance level.

Needless to say, it is obvious from Table 3 and Figs. 6–10, that the DLztd model showed varying performances at the IGS stations with stations BJCO and YKRO, and DAKR and CPVG yielding similar results. The difference

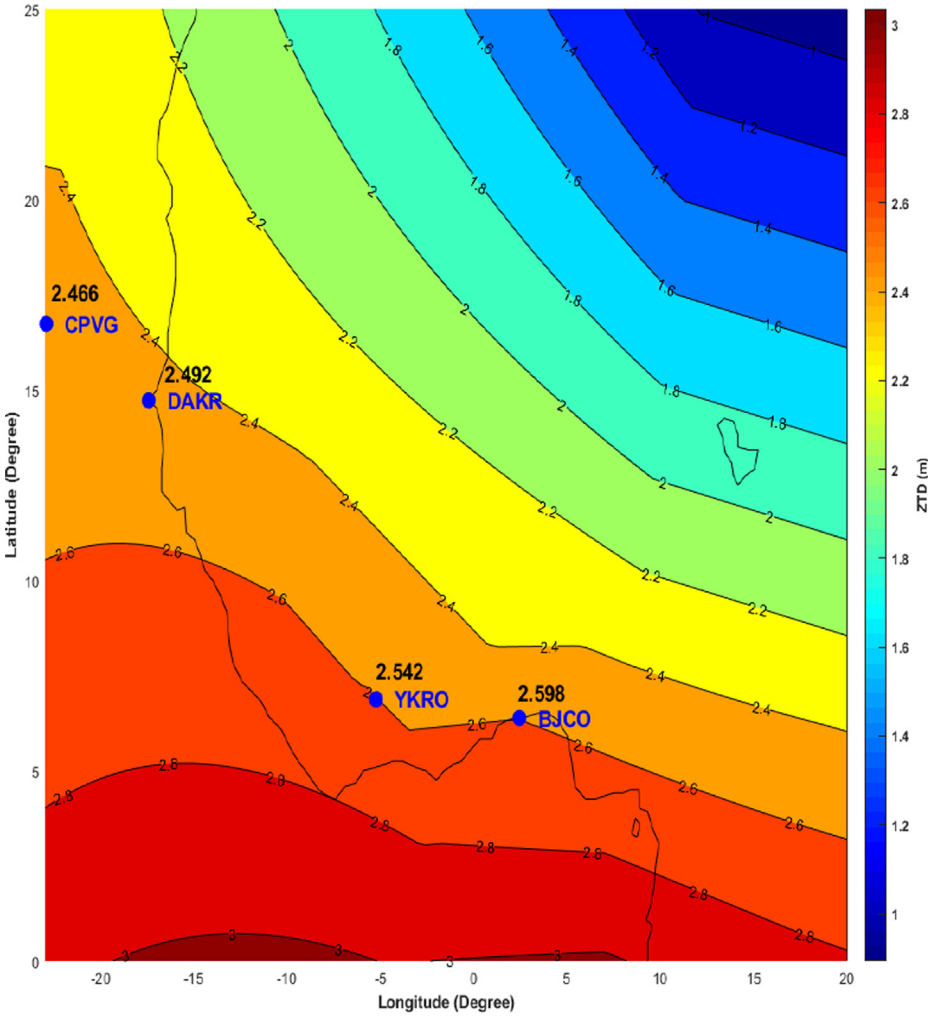

Fig.10. Spatial distribution of ZTD (m) of the study area from 2019. The blue markers/circles represent the IGS stations under study, the black contour lines and the various filled colours represent the variation of the ZTD over the study area, the black irregular shaped line represents the political boundary of West Africa, the black shaped polygon (between contour lines 1.8 and 2) denotes lake chad, the colour scale corresponds to the average ZTD values for 2019. (For interpretation of the references to colour in this figure legend, the reader is referred to the web version of this article.)

in performance at the various stations can be related to the distribution of atmospheric water vapour over the stations which in turn has a significant impact on the ZTD estimation. Atmospheric water vapour is inhomogeneous and highly variable both in space and time which can induce sudden fluctuations in the water vapour content in the atmosphere. These instabilities can further result in an erratic perturbation in ZTD variation, influencing the overall statistics especially the bias and RMSE (Yao et al., 2018a,b; Jiang et al., 2020). According to Zhai & Eskridge (1997), the distribution of atmospheric water vapour is influenced by the geographical latitude of the stations. As the latitude increases, the amount of water vapour decreases, resulting in decreasing the ZTD estimation. Thus, the spatial distribution of ZTD is also associated with latitude (Yao et al., 2018a,b; Chen et al., 2020; Jiang et al., 2020; Ssenyunzi et al., 2020). It can be seen from Fig. 10 that the ZTD increases with decreasing latitude values. The mean ZTD computed at each IGS station for the year 2019 as shown in Fig. 9 reveals that the BJCO station at latitude 6.3847°N has the highest mean ZTD value of about 2.598 m. This is followed by the YKRO station at latitude 6.8706°N having a mean ZTD value of about 2.542 m, then DAKR at latitude 14.7212°N with an average ZTD of 2.492 m. The CPVG station at the highest latitude of 16.7321°N has the least ZTD value of 2.466 m. This result presumes that GNSS stations at low latitude are highly prone to tropospheric effects (Dodo et al., 2019). This can further be seen in Fig. 10 showing the spatial distribution of tropospheric delay in West Africa with emphasis on the West African IGS stations. Fig. 10 shows that IGS stations in West Africa particularly Benin (BJCO) and Cote d'Ivoire (YKRO) are highly liable to the impact of the tropospheric delay compared to DAKR and CPVG in Senegal and Cape Verde respectively. Correspondingly, it is also clear from Table 3 that the mean bias and RMSE values are larger in low latitude stations (BJCO: bias = 5.51 mm, RMSE = 9.87 mm, YKRO: bias = 6.78 mm, RMSE = 11.55 mm) and smaller at high latitude stations (DAKR: bias = 4.50 mm,

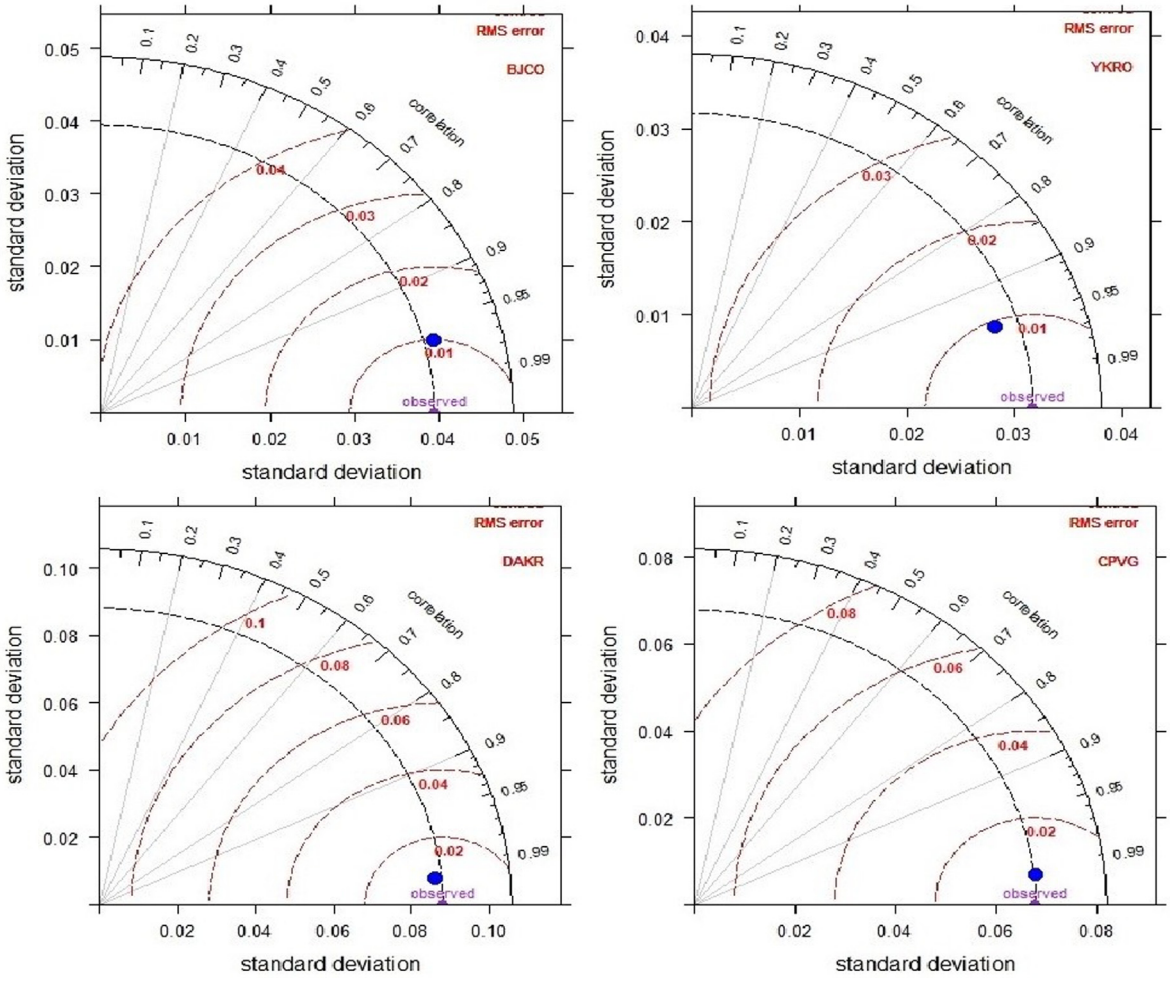

Fig. 11. Taylor's diagram showing a statistical comparison between modelled and IGS values over four IGS stations in West Africa. The blue markers represent the DLztd model and quantify how closely the DLztd predictions at each station match the IGS ZTD values. The red contours or arcs represent the centred RMSE, the black arc with the marked graduated values (0.1–0.99) represent the Pearson correlation coefficient (R), the point labelled "observed" on the x-axis represent the observed (IGS) standard deviation. (For interpretation of the references to colour in this figure legend, the reader is referred to the web version of this article.)

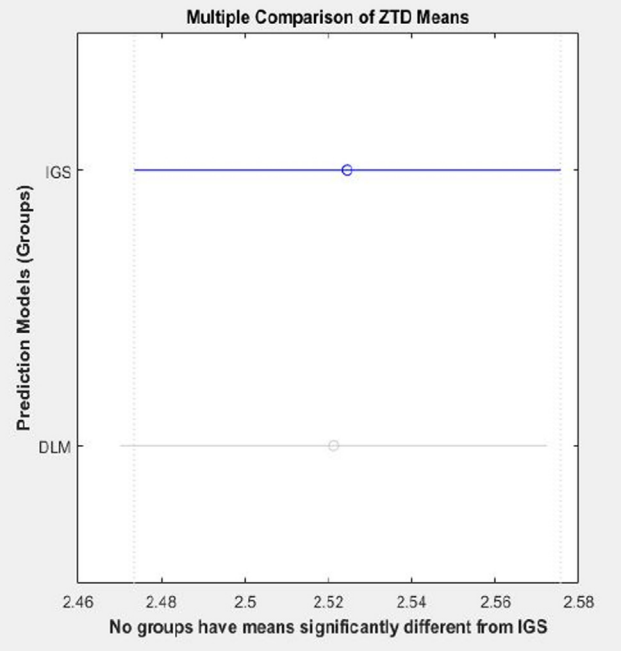

Fig. 12. Multiple Comparison of Groups ZTD Means (unit: m). The small circle symbols (blue and grey) represent the group means, while the bars (horizontal lines) represent the comparison interval.

RMSE = 8.84 mm, CPVG: bias = 2.40 mm, RMSE = 8.22 mm), also implying that the accuracy of ZTD varies in space, which is largely correlated to latitude (Jiang et al., 2020). Thus, the lower the latitude of the station is, the larger the bias and RMSE of the ZTD estimation (Jiang et al., 2020). This is because, at low latitude, the tropospheric activity is strongest compared to stations at high latitude making it difficult to model the ZTD, resulting in the larger bias and RMSE. It can further be observed in Table 3 and Figs. 6, 8, and 11 that all the statistics are showing less good results (large bias and RMSE) for the YKRO station compared to BJCO which is at the lowest latitude. The reason could be related to the climatic conditions of the countries of the two stations (Ssenyunzi and Oruru, 2019). YKRO is located in Cote d'Ivoire while BJCO situated in Benin. The climate of Cote D'Ivoire is characterized by high humidity and rainfall compared to that of Benin. The high humidity or rainfall causes extreme instability in water vapour variation, which in turn increases the difficulty of modelling the ZTD (Jiang et al., 2020) at the YKRO station, hence the large bias and RMS shown at the YKRO station as compared to the BJCO station.

Conclusively, Table 3 also offers the overall average MB: 3.25 mm, RMSE: 9.62 mm, MAPE: 0.30%, R^2: 0.9587, NSE: 0.9466, and FAC2: 1.00 (100%), implying that the DLztd model performed better and satisfies all the thresholds criteria for an ideal model. This as well demonstrates that the proposed DLztd model can effectively improve the accuracy of the ZTD prediction in West Africa.

5. Conclusions

Deep learning is more and more being recognized as an important tool for artificial intelligence (AI) research in recent years, with applications in several fields to finding solutions to a variety of problems. In GNSS applications, the tropospheric delay is being considered the major error source and a growing concern to GNSS users. Over the years, precise modelling of the tropospheric delay has become one of the research hotspots among the GNSS research community, inspiring several techniques towards the precise estimation and mitigation of the tropospheric delay. In this study, we developed a deep learning ZTD (DLztd) prediction model using TensorFlow and Keras for predicting daily IGS final ZTD. Daily surface meteorological parameters comprising of Pressure (P), Temperature (T), and Water vapour partial pressure (e), as well as daily ZTD and station coordinates (latitude (φ), and ellipsoidal height (h)) obtained from the site-wise VMF3 ZTD products for global IGS stations for the period 2015–2018 were used as input variables to train and test the model, while data from 2019 covering four IGS stations (BJCO, CPVG, DAKR, and YKRO) were used to evaluate the predictive performance of the developed DLztd model. Statistical performance indicators such as MB, RMSE, MAPE, R^2, NSE, and FAC2 as well as graphical illustrations such as scatterplots, residual plots, time variation plots, and Taylor's diagram and non-parametric multiple comparison test (MCT) were employed to determine the degree of agreement between the DLztd model predictions and IGS final ZTD data. The results from the various analyses indicate exceptionally good prediction capability of the DLztd model with average MB, RMSE, MAPE, R^2, NSE and FAC2 of 3.25 mm, 9.62 mm, 0.30%, 0.959, 0.947, and 1.00 respectively, proving high prediction accuracy by the model, as this is in accordance with (Chiew and McMahon, 1993; Yadav and Chandel, 2014; Moriasi et al., 2015) thresholds criteria for a perfect model. The findings of this study demonstrate that the DLztd model can be implemented as an alternative source for predicting daily IGS-ZTD for both GNSS positioning and meteorological applications in West Africa, and also as a means of improving the continuous availability of the IGS-ZTD data over the IGS stations under study just in case the stations' ZTD data are unavailable.

Declaration of Competing Interest

The authors declare that they have no known competing financial interests or personal relationships that could have appeared to influence the work reported in this paper.

Acknowledgments

The authors wish to thank the Vienna Mapping Functions (VMF) and International GNSS Service (IGS) data centres for their open access tropospheric delay products.

We also want to express our gratitude to our research assistants Solomon Acheampong and Charles Gameti of KNUST for respectively assisting us with the python programming and the workflow methodology flowchart.

References

Abadi, M. et al., 2016 TensorFlow: Large-Scale Machine Learning on Heterogeneous Distributed Systems. Available at: https://arxiv.org/abs/1603.04467.

Abdel-Sattar, M., Aboukarima, A.M., Alnahdi, B.M., 2021. Application of artificial neural network and support vector regression in predicting mass of ber fruits (Ziziphus mauritiana Lamk.) based on fruit axial dimensions. PLoS ONE 16 (1 January), 1–15. https://doi.org/10.1371/journal.pone.0245228.

Afzaal, H., Farooque, A.A., Abbas, F., Acharya, B., Esau, T., 2020. Groundwater Estimation from Major Physical Hydrology Components Using Artificial Neural Networks and Deep Learning. Water 12 (5).

Agarap, A. F. (2018) Deep Learning using Rectified Linear Units (ReLU), arXiv preprint arXiv. Available at: https://arxiv.org/pdf/1803.08375.

Ahmadi, H., Rodehutscord, M., 2017. Application of Artificial Neural Network and Support Vector Machines in Predicting Metabolizable Energy in Compound Feeds for Pigs. Front. Nutrition 4 (27), 1–8. https://doi.org/10.3389/fnut.2017.00027.

Ali, M.H., Abustan, I., 2014. A new novel index for evaluating model performance. J. Natural Resour. Develop. 4 (1), 1–9. https://doi.org/10.5027/jnrd.vi0.01.

Anantrasirichai, N., Biggs, J., Albino, F., Bull, D., 2019. A deep learning approach to detecting volcano deformation from satellite imagery using synthetic datasets. Remote Sens. Environ. Elsevier 230. https://doi.org/10.1016/j.rse.2019.04.032 111179.

Askne, J., Nordius, H., 1987. Estimation of tropospheric delay for microwaves from surface weather data. Radio Sci. Wiley Online Library 22 (3), 379–386.

Bevis, M., Businger, S., Chiswell, S., Herring, T.A., Anthes, R.A., Rocken, C., Ware, R.H., 1994. GPS meteorology: Mapping zenith wet delays onto precipitable water. J. Appl. Meteorol. 33 (3), 379–386.

Bevis, M., Businger, S., Herring, T.A., Rocken, C., Anthes, R.A., Ware, R.H., 1992. 'GPS meteorology: Remote sensing of atmospheric water vapor using the Global Positioning System', *Journal of Geophysical Research: Atmospheres*. Wiley Online Library 97 (D14), 15787–15801.

Bianchi, C. E., Mendoza, L. P. O., Fernández, L. I., Natali, M. P., Meza, A. M. and Moirano, J. F. (2016) 'Multi-year GNSS monitoring of atmospheric IWV over Central and South America for climate studies', in Annales Geophysicae. doi: 10.5194/angeo-34-623-2016.

Biondi, D., Freni, G., Iacobellis, V., Mascaro, G., Montanari, A., 2012. 'Validation of hydrological models : Conceptual basis, methodological approaches and a proposal for a code of practice', Physics and Chemistry of the Earth. Elsevier Ltd 42–44, 70–76. https://doi.org/10.1016/j.pce.2011.07.037.

Black, H.D., 1978. An easily implemented algorithm for the tropospheric range correction. J. Geophys. Res. Solid Earth Wiley Online Library 83 (B4), 1825–1828.

Boehm, J., Kouba, J., Schuh, H., 2009. Forecast Vienna Mapping Functions 1 for real-time analysis of space geodetic observations. J. Geod. 83, 397–401. https://doi.org/10.1007/s00190-008-0216-y.

Boehm, J. and VanDam, T., 2009. 'Modeling deficiencies and modeling based on external data', in Second GGOS unified analysis workshop, IERS, Grand Hyatt, San Francisco, CA, USA, December, pp. 11–12.

Byun, S. H., Bar-sever, Y. E. and Gendt, G., 2005. 'The New Tropospheric Product of the International GNSS Service', in In: Proceedings of the ION GNSS-2005 18th International Technical Meeting of The Satellite Division of The Institute of Navigation. Long Beach, CA, pp. 241–249.

Chandrasekaran, S., 2019. Deep Learning Approach for Customer Records Prediction for Future Products Issues. J. Comput. Commun. Sci. Res. Publishing 07, 44–54. https://doi.org/10.4236/jcc.2019.73005 M4 - Citavi.

Chang, J.C., Hanna, S.R., 2004. Air quality model performance evaluation. Meteorol. Atmos. Phys. Springer 87 (1–3), 167–196. https://doi.org/10.1007/s00703-003-0070-7.

Chen, P., Ma, Y., Liu, H. and Zheng, N. (2020) 'A new global tropospheric delay model considering the spatiotemporal variation characteristics of ZTD with altitude coefficient', Earth and Space Science, 7(4), p. e2019EA000888. doi: 10.1029/2019ea000888.

Chiew, F.H.S., McMahon, T.A., 1993. Assessing the adequacy of catchment streamflow yield estimates. Soil Res. CSIRO 31 (5), 665–680. https://doi.org/10.1071/sr9930665.

Ding, M. and Hu, W., 2019. 'Erratum and addendum to the paper "A new ZTD model based on permanent ground-based GNSS-ZTD data", Survey Review, 2016, 48(351), 385–391', Survey Review, 51(366), pp. 280–287. doi: 10.1080/00396265.2017.1420585.

Ding, Maohua, Hu, W., Jin, X., Yu, L., 2016. A new ZTD model based on permanent ground- based GNSS-ZTD data. Survey Review 48 (351), 385–391. https://doi.org/10.1179/1752270615Y.0000000034.

Dodo, J.D., Ekeanyanwu, U.O., Ono, M.N., 2019. Evaluation of Five Tropospheric Delay Models on Global Navigation Satellite System Measurements in Southern Nigeria. J. Geosci. 7 (4), 201–211.

Feng, P., Li, F., Yan, J., Zhang, F., Barriot, J.-P., 2020. Assessment of the Accuracy of the Saastamoinen Model and VMF1/VMF3 Mapping Functions with Respect to Ray-Tracing from Radiosonde Data in the Framework of GNSS Meteorology. Remote Sens. Multidisciplinary Digital Publishing Inst. 12 (20), 3337. https://doi.org/10.3390/rs12203337 M4 - Citavi.

Fox, D.G., 1981. Judging Air Quality Model Performance: a summary of the ams workshop on dispersion model performance, woods hole, mass. Bull. Am. Meteorol. Soc. 62 (5), 599–609.

Frost, J., 2019. Regression Analysis: An Intuitive Guide for Using and Interpreting Linear Models. Statistics By Jim Publishing.

Goodfellow, I., Bengio, Y., Courville, A., 2016. Deep learning (The Adaptive Computation and Machine Learning Series). MIT press.

GoogleMap, 2021. 'Map of West Africa'. Available at: https://www.-google.com/maps/place/West+Africa/@13.8776241,-19.2126827,4z/data Aceessed on 02/18/2021.

Gulli, A., Pal, S., 2017. Deep learning with Keras. Packt Publishing Ltd..

Hadas, T., Kaplon, J., Bosy, J., Sierny, J., Wilgan, K., 2013. Near-real-time regional troposphere models for the GNSS precise point positioning technique. Meas. Sci. Technol. IOP Publishing 24 (5), 55003. https://doi.org/10.1088/0957-0233/24/5/055003.

Hadas, T., Teferle, F.N., Kazmierski, K., Hordyniec, P., Bosy, J., 2017. Optimum stochastic modeling for GNSS tropospheric delay estimation in real-time. GPS Solut.. Springer 21 (3), 1069–1081.

Hobiger, T., Ichikawa, R., Takasu, T., Koyama, Y., Kondo, T., 2008. Ray-traced troposphere slant delays for precise point positioning. Earth Planets Space 60 (5), 1–4. https://doi.org/10.1186/bf03352809.

Hofmann-Wellenhof, B., Lichtenegger, H., Wasle, E., 2008. GNSS — Global Navigation Satellite Systems GPS. GLONASS, Galileo, and more. https://doi.org/10.1007/978-3-211-73017-1.

Hopfield, H.S., 1969. 'Two-quartic tropospheric refractivity profile for correcting satellite data. J. Geophys. Res. Wiley Online Library 74 (18), 4487–4499. https://doi.org/10.1029/JC074i018p04487.

Isioye, O.A., Combrinck, L., Botai, J.O., Munghemezulu, C., 2015. The potential for observing African weather with GNSS remote sensing. Adv. Meteorol. Hindawi 2015, 1–16.

Jgouta, M., Nsiri, B. and Marrakh, R. (2016) 'Usage of a Correction Model to Enhance the Evaluation of the Zenith Tropospheric Delay Usage of a Correction Model to Enhance the Evaluation of the Zenith Tropospheric Delay', (April).

Jiang, C., Xu, T., Wang, S., Nie, W., Sun, Z., 2020. Evaluation of Zenith Tropospheric Delay Derived from ERA5 Data over China Using GNSS Observations. Remote Sens. Multidisciplinary Digital Publish. Inst. 12 (4), 663. https://doi.org/10.3390/rs12040663.

Kleijer, F. (2004) Troposphere Modeling and Filtering for Precise GPS Leveling, Netherlands Geodetic Commission.

Kumar, A., Bellam, N.K., Sud, A., 1999. Performance of an Industrial Source Complex Model: Predicting long-term concentrations in an urban area. Environ. Prog. 18 (2), 93–100. https://doi.org/10.1002/ep.670180213.

Landskron, D., Böhm, J., 2018. VMF3/GPT3: refined discrete and empirical troposphere mapping functions. J. Geodesy Springer Berlin Heidelberg 92 (4), 349–360. https://doi.org/10.1007/s00190-017-1066-2.

Leandro, R.F., Langley, R.B., Santos, M.C., 2008. UNB3m_pack: A neutral atmosphere delay package for radiometric space techniques. GPS Solutions 12 (1), 65–70. https://doi.org/10.1007/s10291-007-0077-5.

Lee, S., Lee, D.K., 2018. 'What is the proper way to apply the multiple comparison test? Korean J. Anesthesiol. Korean Soc. Anesthesiolog. 71 (5), 353–360. https://doi.org/10.4097/kja.d.18.00242.

Legates, D. R. and Mccabe, G. J., 2013. 'Short Communication A refined index of model performance : a rejoinder', 1056(April 2012), pp. 1053–1056. doi: 10.1002/joc.3487.

Lewis, C. (1982) 'International and Business Forecasting Methods Butterworths: London'.

Li, L., Xu, Y., Yan, L., Wang, S., Liu, G., Liu, F., 2020. A Regional NWP Tropospheric Delay Inversion Method Based on a General Regression Neural Network Model. Sensors. Multidisciplinary Digital Publishing Institute, p. 3167, 10.3390/s20113167.

Liu, Y.H., Maldonado, P., 2018. R Deep Learning Projects: Master the techniques to design and develop neural network models in R. Packt Publishing Ltd..

Malekmohamadi, I., Bazargan-Lari, M.R., Kerachian, R., Nikoo, M.R., Fallahnia, M., 2011. Evaluating the efficacy of SVMs, BNs, ANNs and ANFIS in wave height prediction. Ocean Eng. Elsevier 38 (2–3), 487–497. https://doi.org/10.1016/j.oceaneng.2010.11.020.

Manaswi, N. K. (2018) 'Understanding and Working with Keras', in Deep Learning with Applications Using Python. Apress, Berkeley, CA, pp. 31–43. doi: 10.1007/978-1-4842-3516-4_2 M4 - Citavi.

McHugh, M.L., 2011. Multiple comparison analysis testing in ANOVA. In: Biochemia medica: Biochemia medica. Medicinska naklad. a, pp. 203–209, 10.11613/BM.2011.029.

Mendes, V. B., 1999. Modeling the neutral-atmospheric propagation delay in radiometric space techniques, UNB geodesy and geomatics engineering technical report. Department of Geodesy and Geomatics Engineering Technical Report No. 199, University of New Brunswick, Fredericton, New Brunswick, Canada, 353 pp.

Meunram, P., Satirapod, C., 2019. Spatial variation of precipitable water vapor derived from GNSS CORS in Thailand. Geod. Geodyn. Elsevier 10 (2), 140–145. https://doi.org/10.1016/j.geog.2019.01.003.

Moriasi, D.N., Gitau, M.W., Pai, N., Daggupati, P., 2015. Hydrologic and water quality models: Performance measures and evaluation criteria. In: Transactions of the ASABE American Society of Agricultural and Biological Engineers, pp. 1763–1785, 10.13031/trans.58.10715.

Nash, E., Sutcliffe, V., 1970. River flow forecasting through conceptual models part I—A discussion of principles. J. Hydrol. 10 (3), 282–290.

Nikolaidou, T., Balidakis, K., Nievinski, F., Santos, M., Schuh, H., 2018. Impact of different NWM-derived mapping functions on VLBI and GPS analysis. Earth Planets Space 70 (1), 95. https://doi.org/10.1186/s40623-018-0865-x.

Penna, N., Dodson, A., Chen, W., 2001. Assessment of EGNOS tropospheric correction model. J. Navigat. Cambridge Univ. Press 54 (1), 37–55.

Pikridas, C., Katsougiannopoulos, S., Ifadis, I.M., 2010. Predicting Zenith Tropospheric Delay using the Artificial Neural Network technique. Application to selected EPN stations. J. Natl Cancer Inst. 88 (24), 1803–1805.

Prakash, P.K.S., Rao, A.S.K., 2017. R deep learning cookbook. Packt Publishing Ltd..

Putri, N., Landskron, D., Böhm, J., 2020. Assessing the performance of Vienna Mapping Functions 3 for GNSS stations in Indonesia using Precise Point Positioning. Adv. Geosci. 50, 77–86. https://doi.org/10.5194/adgeo-50-77-2020.

Saastamoinen, J., 1972. Atmospheric correction for the troposphere and stratosphere in radio ranging satellites. In: The use of artificial satellites for geodesy Wiley Online Library, pp. 247–251.

Sanlioglu, I. and Zeybek, M., 2012. Investigation On GPS Heighting Accuracy With Use Of Tropospheric Models In Commercial GPS Softwares For Different Heights', in FIG Working Week 2012, At Rome, Italy, Volume: TS09B - Precise Point Positioning, 6080, pp. 6–10.

Sanz, J., Juan, J. M. and Hernández-Pajares, M., 2013. 'GNSS data processing, Vol. I: fundamentals and algorithms', Noordwijk, the Netherlands: ESA Communications, ESTEC TM-23/l.

Sayegh, A.S., Munir, S., Habeebullah, T.M., 2014. Comparing the performance of statistical models for predicting PM10 concentrations. Aerosol Air Qual. Res. 14 (3), 653–665. https://doi.org/10.4209/aaqr.2013.07.0259.

Shirke, V., Walika, R. and Tambade, L., 2018. 'Drop: A Simple Way to Prevent Neural Network by Overfitting', International Journal of Research in Engineering, Science and Management, 1(9), pp. 2581–5782. Available at: https://www.ijresm.com/vol_1_2018/vol1_iss9_september18/ijresm_19_24.pdf TS - RIS M4 - Citavi.

Smith, E.K., Weintraub, S., 1953. The constants in the equation for atmospheric refractive index at radio frequencies. J. Res. Notional Bureau Standards 50 (1), 39–41.

Srivastava, N., Hinton, G., Krizhevsky, A., Sutskever, I. and Salakhutdinov, R., 2014. 'Dropout: a simple way to prevent neural networks from overfitting', The journal of machine learning research, 15(1), pp. 1929–1958. Available at: https://www.jmlr.org/papers/volume15/srivastava14a/srivastava14a.pdf?utm_campaign=buffer&utm_content=buffer79b43&utm_medium=social&utm_ source=twitter.com.

Ssenyunzi, R.C. et al., 2020. Performance of ERA5 data in retrieving Precipitable Water Vapour over East African tropical region. Adv. Space Res. COSPAR 65 (8), 1877–1893. https://doi.org/10.1016/j.asr.2020.02.003.

Ssenyunzi, R. C., Oruru, B., D'ujanga, F. M., Realini, E., Barindelli, S., Tagliaferro, G. and van de Giesen, N., 2019. 'Variability and accuracy of Zenith Total Delay over the East African Tropical Region', Advances in Space Research. Elsevier. 64 (4) 900–920 doi: https://doi.org/10.1016/j.asr.2019.05.027.

Suleiman, A., Tight, M.R., Quinn, A.D., 2014. Extensive Evaluation of Neural Network Based PM 10 Prediction Models Using Openair Package. In: 20th International Transport and Air Pollution Conference 2014, pp. 1–14.

Sun, J., Wu, Z., Yin, Z. and Ma, B. (2017) 'A simplified GNSS tropospheric delay model based on the nonlinear hypothesis', GPS Solutions. School of Electronics and Information Engineering, Harbin Institute of Technology, Harbin, China wuzhilu@hit.edu.cn China Academy of Space Technology, Beijing, China M4 - Citavi: Springer, 21(4), pp. 1735–1745. doi: 10.1007/s10291-017-0644-3.

Suparta, W., Alhasa, K.M., 2013. Application of ANFIS model for prediction of zenith tropospheric delay. Information Technology and Biomedical Engineering (ICICI-BME), pp. 172–177. https://doi.org/10.1109/ICICI-BME.2013.6698487.

Suparta, W., Alhasa, K.M., 2015. Modeling of zenith path delay over Antarctica using an adaptive neuro fuzzy inference system technique. Expert Syst. Appl. Elsevier 42 (3), 1050–1064. https://doi.org/10.1016/j.eswa.2014.09.029.

Suparta, W., Alhasa, K.M., 2016. Modeling of tropospheric delays using ANFIS. Springer.

Taylor, K.E., 2001. 'Summarizing multiple aspects of model performance in a single diagram', *Journal of Geophysical Research: Atmospheres*. Wiley Online Library 106 (D7), 7183–7192. https://doi.org/10.1029/2000JD900719.

Tesmer, V., Boehm, J., Heinkelmann, R., Schuh, H., 2007. Effect of different tropospheric mapping functions on the TRF, CRF and position time-series estimated from VLBI. J. Geod. 81 (6–8), 409–421. https://doi.org/10.1007/s00190-006-0126-9.

Tosun, E., Aydin, K., Bilgili, M., 2016. 'Comparison of linear regression and artificial neural network model of a diesel engine fueled with biodiesel-alcohol mixtures', *Alexandria Engineering Journal*. Faculty of Engineering, Alexandria University 55 (4), 3081–3089. https://doi.org/10.1016/j.aej.2016.08.011.

Urquhart, L., Santos, M., Nievinski, F., Böhm, J., 2014. Generation and Assessment of VMF1-Type Grids Using North-American Numerical Weather Models. Int. Assoc. Geodesy Symposia 139, 3–9. https://doi.org/10.1007/978-3-642-37222-3_1.

Walpersdorf, A., Bouin, M.-N., Bock, O., Doerflinger, E., 2007. Assessment of GPS data for meteorological applications over Africa: Study of error sources and analysis of positioning accuracy. J. Atmos. Sol. Terr. Phys. 69 (12), 1312–1330. https://doi.org/10.1016/j.jastp.2007.04.008.

Wang, Y., Li, Y., Song, Y., Rong, X., 2020. The Influence of the Activation Function in a Convolution Neural Network Model of Facial Expression Recognition. Appl. Sci. Multidisciplinary Digital Publishing Inst. 10 (5), 1897. https://doi.org/10.3390/app10051897 M4 - Citavi.

Weyn, J.A., Durran, D.R., Caruana, R., 2019. Can machines learn to predict weather? Using deep learning to predict gridded 500-hPa geopotential height from historical weather data. J. Adv. Model. Earth Syst. Wiley Online Library 11 (8), 2680–2693. https://doi.org/10.1029/2019MS001705.

Yadav, A.K., Chandel, S.S., 2014. 'Solar radiation prediction using Artificial Neural Network techniques: A review. Renew. Sustain. Energy Rev. Elsevier 33, 772–781. https://doi.org/10.1016/j.rser.2013.08.055.

Yang, Y. et al., 2017. A new regional tropospheric delay correction model based on BP neural network. In: 2017 Forum on Cooperative Positioning and Service (CPGPS). IEEE, pp. 96–100, 10.1109/CPGPS.2017.8075104.

Yao, Y.-B., He, C.-Y., Zhang, B., Xu, C.-Q., 2018a. A new global zenith tropospheric delay model GZTD. Chinese J. Geophys. 56 (7), 2218–2227. https://doi.org/10.6038/cjg20130709.

Yao, Y., Xu, X., Hu, Y., 2017. Precision Analysis of GGOS Tropospheric Delay Product and Its Application in PPP. Acta Geodaetica et Cartographica Sinica 46 (3), 278–287. https://doi.org/10.11947/j.AGCS.2017.20160383.

Yao, Y., Xu, X., Xu, C., Peng, W., Wan, Y., 2018b. 'GGOS tropospheric delay forecast product performance evaluation and its application in real-time PPP. J. Atmospheric Solar-Terrestrial Phys. Elsevier Ltd 175 (2018), 1–17. https://doi.org/10.1016/j.jastp.2018.05.002.

Younes, S.A.-M., 2016. 'Modeling investigation of wet tropospheric delay error and precipitable water vapor content in Egypt. Egyptian J. Remote Sens. Space Sci. Elsevier 19 (2), 333–342. https://doi.org/10.1016/j.ejrs.2016.05.002.

Zhai, P., Eskridge, R.E., 1997. Atmospheric water vapor over China. J. Clim. 10 (10), 2643–2652. https://doi.org/10.1175/1520-0442(1997)010<2643:AWVOC>2.0.CO;2.

Zhang, H., Yuan, Y., Li, W., Li, Y., Chai, Y., 2016. Assessment of three tropospheric delay models (IGGtrop, EGNOS and UNB3m) based on precise point positioning in the Chinese region. Sensors. Multidisciplinary Digital Publishing Inst. 16 (1), 122.

Zhang, Q., Li, F., Zhang, S., Li, W., 2020. Modeling and forecasting the gps zenith troposphere delay inwest antarctica based on different blind source separation methods and deep learning. Sensors 20 (8). https://doi.org/10.3390/s20082343.

Zhao, Q., Yao, Y., Yao, W., Li, Z., 2018. Real-time precise point positioning-based zenith tropospheric delay for precipitation forecasting. Sci. Rep. 8 (1), 1–12. https://doi.org/10.1038/s41598-018-26299-3.

Zheng, D.Y., Hu, W.S., Wang, J., Zhu, M.C., 2015. Research on regional zenith tropospheric delay based on neural network technology. Survey Review 47 (343), 286–294. https://doi.org/10.1179/1752270614Y.0000000130.

Zhou, F., Cao, X., Ge, Y., Li, W., 2020. Assessment of the positioning performance and tropospheric delay retrieval with precise point positioning using products from different analysis centers. GPS Solut. Springer 24 (1), 12. https://doi.org/10.1007/s10291-019-0925-0.

Zhu, Q., Zhao, Z., Lin, L., Wu, Z., 2010. Accuracy improvement of zenith tropospheric delay estimation based on GPS precise point positioning algorithm. Geo-Spatial Info. Sci. 13 (4), 306–310. https://doi.org/10.1007/s11806-010-0400-0.